

# Evolution of a stratified rotating shear layer with horizontal shear. Part 2. Nonlinear evolution

Eric Arobone and Sutanu Sarkar†

Department of Mechanical and Aerospace Engineering, University of California San Diego,  
CA 92093, USA

(Received 3 March 2013; revised 25 May 2013; accepted 21 July 2013;  
first published online 6 September 2013)

Direct numerical simulation is used to investigate the nonlinear evolution of a horizontally oriented mixing layer with uniform stable stratification and coordinate system rotation about the vertical axis. The important dimensional parameters governing inviscid dynamics are maximum shear  $S(t)$ , buoyancy frequency  $N$ , angular velocity of rotation  $\Omega$  and characteristic shear thickness  $L(t)$ . The effect of rotation rate,  $\Omega$ , on the development of fluctuations in the shear layer is systematically studied in a regime of strong stratification. An instability mechanism, qualitatively distinct from the inertial instability, is found to deform columnar vortex cores in vertical planes for a strongly stratified rotating mixing layer. This mechanism emerges when centreline absolute vertical vorticity,  $\langle \omega_3 \rangle(t) + 2\Omega$ , is nearly zero as predicted by the linear stability analysis in Part 1 (*J. Fluid Mech.*, vol. 703, 2012, pp. 29–48). When the initial rotation rate is moderately anticyclonic, strong destabilization and a cascade to small scales is observed, consistent with prior studies involving horizontally sheared flow in the presence of rotation. Examination of enstrophy budgets in cases which are initially inertially unstable reveal the importance of baroclinic torque in maintaining lateral enstrophy fluctuations substantially beyond the time when the flow becomes inertially stable. The cyclonic stratified cases show weak nonlinearity in vortex dynamics. At high Reynolds number, despite the strong stratification, the flow exhibits three-dimensional, nonlinear dynamics and significant vertical mixing except for cases where the rotation is stabilizing.

**Key words:** rotating turbulence, stratified turbulence, turbulent flows

---

## 1. Introduction

The effects of strong stratification and moderate coordinate system rotation rates, where  $Fr_h = S/N \lesssim O(1)$  and  $Ro = S/2\Omega \sim O(1)$ , on shear flow is important for basic understanding of submesoscale ocean dynamics. Here,  $Fr_h$ , is the horizontal Froude number,  $Ro$  is the Rossby number, and  $S$  the maximum shear,  $N$  the buoyancy frequency and  $\Omega$  the angular velocity of rotation. This study explores a horizontally oriented hyperbolic-tangent mixing layer including stratification and rotation effects. Isolated horizontal shear is prevalent in boundary currents and in the wake of isolated topography. Previous work has explored the nonlinear evolution of horizontally oriented shear layers subjected to rotation (Métais *et al.* 1995; Potylitsin

† Email address for correspondence: [ssarkar@ucsd.edu](mailto:ssarkar@ucsd.edu)

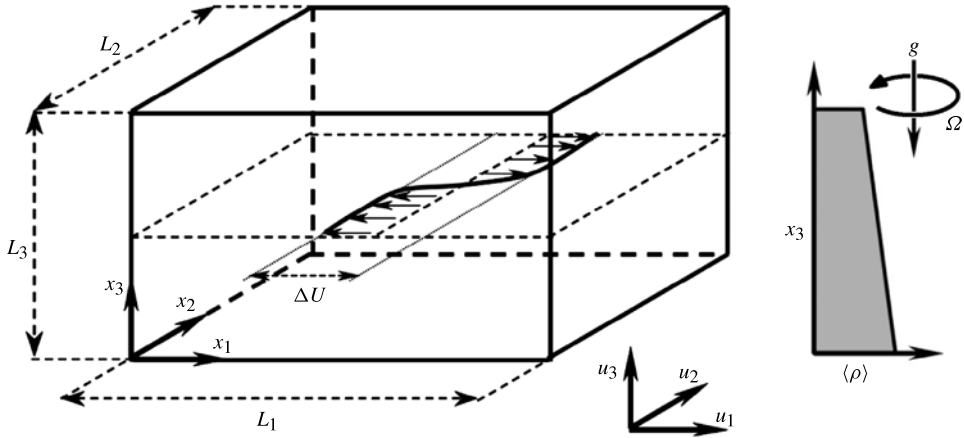


FIGURE 1. Schematic of the rotating stratified horizontal shear layer. Additional relevant parameters include the vorticity thickness  $\delta_\omega = \Delta U / |\langle \omega_3 \rangle|_{max}$ , kinematic viscosity  $\nu$ , scalar diffusivity  $\kappa$  and reference density  $\rho_0$ . Cyclonic rotation refers to cases where centreline  $\langle \omega_3 \rangle$  and  $\Omega$  have the same sign, while anticyclonic rotation refers to cases where they have opposite signs.

& Peltier 2003) or stratification (Basak & Sarkar 2006; Arobone & Sarkar 2010) alone, but not in combination. Figure 1 gives a schematic illustrating the rotating stratified horizontal shear layer and relevant dimensional parameters.

In Part 1 (Arobone & Sarkar 2012) the effect of rotation and stratification on growth rates for linear evolution of exponentially growing modes was explored for a horizontal shear layer. The unstratified rotating shear layer is known to be susceptible to inertial (i.e. centrifugal) instability, that is typically manifested as overturning motions with low streamwise wavenumber, and the barotropic instability associated with horizontal shear that is manifested as vortex trains such as Kelvin–Helmholtz (KH) billows. Stratification acted to stabilize the inertial instability for moderate values of  $Ri_b^{-1/2}k_3$ , where  $Ri_b = N^2/S^2$  is the Richardson number and  $k_3$  the vertical wavenumber, and increased the range of vertical wavenumbers associated with both inertial and barotropic instability. When the absolute vertical vorticity,  $\langle \omega_3 \rangle + 2\Omega = -S + 2\Omega$ , was nearly zero at the centreline, a new instability was found to occur whereby a much larger range of vertical scales was destabilized relative to the non-rotating case as seen in figure 2. Note that the inertial instability of rotating flows is inoperative for  $-S + 2\Omega \geq 0$ . Lastly, self-similar regimes were observed when stratification was strong ( $Ri_b \geq 1$ ) and/or the rotation rate was rapid ( $|2\Omega/S| \gg 1$ ). In the present paper, we assess the role of buoyancy during the *nonlinear* evolution of the stratified rotating shear layer through direct numerical simulation (DNS).

The horizontally oriented shear layer under the influence of rotation alone and without stratification was explored by Métais *et al.* (1995) using direct and large-eddy simulations. The Reynolds number based on free-stream velocity difference and initial vorticity thickness was  $Re = 100$  and a  $64^3$  grid was used. In cases with cyclonic rotation (and anticyclonic rotation when  $|Ro(t)| \leq 1$ ) three-dimensionality was inhibited, consistent with the Taylor–Proudman theorem. For weaker anticyclonic rotation, the flow was strongly destabilized with maximum destabilization achieved when  $Ro \approx -2.5$ , consistent with the linear theory of Yanase *et al.* (1993). In the

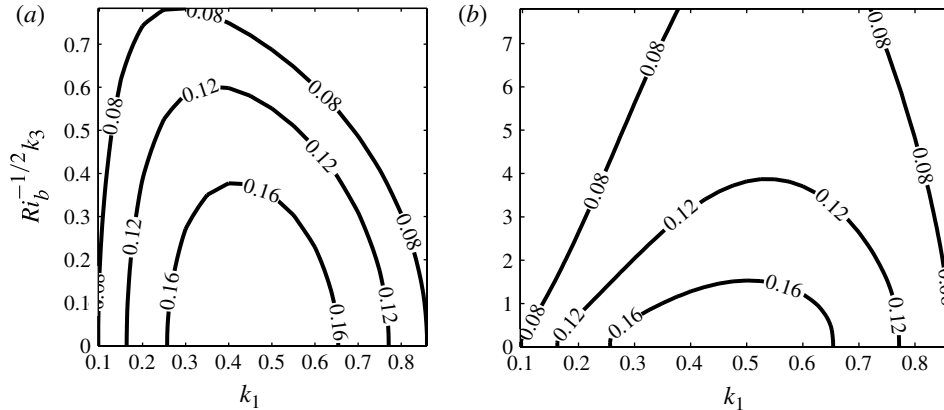


FIGURE 2. Contours of growth rate for linear stability of the stratified horizontal shear layer for (a) the non-rotating case,  $Ri_b = 4$ ,  $2\Omega = 0$ , and (b) the zero absolute vorticity case  $Ri_b = 10$ ,  $2\Omega = -1$ , based on the results of Part 1 (Arobone & Sarkar 2012).

strongly destabilized cases, the vorticity in the shear layer evolved to a collection of strong longitudinal vortex tubes, slightly inclined with respect to vertical. KH rollers were suppressed, yet more enstrophy resulted than in the non-rotating case. The weak anticyclonic cases approached a state of near-constant shear with approximately zero absolute vorticity. Vertical vorticity was proposed to be destroyed via the weak absolute vorticity stretching mechanism of Lesieur, Yanase & Métais (1991).

The effect of stratification alone without system rotation on a horizontally oriented shear layer was explored by Basak & Sarkar (2006) and Arobone & Sarkar (2010) using DNS. The structural organization of vorticity and density fields was the focus of Basak & Sarkar (2006). In strongly stratified cases, columnar vortex cores emerged from an initially turbulent state and subsequently dislocated forming a lattice of ‘pancake’ eddies with large vertical shear and density gradients between the pancakes. The vertical length of vortex cores was found to be proportional to  $\Delta U/N$  where  $\Delta U$  denotes the imposed velocity difference and  $N$  the uniform stratification. Density intrusions and internal gravity waves were observed away from the sheared region. Arobone & Sarkar (2010) extended this work, focusing on statistics and the role of coherent vortical structures. Many statistics, such as turbulent stresses, approached self-similar profiles once  $Ri_b(t) \gg 1$ . For large  $Ri_b$ , transport of density fluctuations was strongly counter-gradient in sharp contrast with the co-gradient transport of a passive tracer observed in the unstratified case. In strongly stratified cases coherent structure evolution exhibited vortical structure reminiscent of the zigzag instability (Billant & Chomaz 2000).

There are observations of asymmetry between cyclonic and anticyclonic vortices in geophysical flows, e.g. figure 1 of Potylitsin & Peltier (1998) which shows asymmetry of the von Kármán vortex street in the lee of mountains on the island of Jan Mayen. Flament *et al.* (2001) observed a horizontal shear layer, containing anticyclonic vortices having  $\omega_3 \sim -f$ , where  $f$  is the Coriolis parameter, forming in the westward North Equatorial Current past the island of Hawaii. The shear layer grew in thickness owing to pairing of these anticyclonic vortices. It was suggested that stronger vortices were not observed due to inertial instability. Anticyclones are quite difficult to generate in the laboratory in a homogeneous fluid, e.g. Kloosterziel & van Heijst (1991) and

Afanasyev & Peltier (1998). In the latter publication the inertial instability was clearly demonstrated for various values of  $Ro$  through novel experimental techniques.

Numerical experiments have also shown asymmetry between cyclones and anticyclones for moderate rotation rates. Bartello, Métais & Lesieur (1994) used numerical simulation to examine the three-dimensionalization of initially quasi-two-dimensional flow along with the two-dimensionalization of initially isotropic three-dimensional flow in an unstratified background. Without rotation, three-dimensionalization of all initially quasi-two-dimensional vortices was observed. When the Coriolis parameter matched  $[\omega_{2D}]_{rms}$  a rapid destabilization of anticyclones occurred; however both cyclones and anticyclones remained stable for more rapid rotation rates. Forced three-dimensional rotating stratified isotropic turbulence was investigated numerically by Smith & Waleffe (2002). Forcing was localized at a large wavenumber. When  $Fr$  was less than a critical value, energy transferred from small to large scales. For  $N/f \gg 2$ , large-scale flow arose as vertically sheared horizontal flow with potential vorticity (PV) modes playing a secondary role. For  $1/2 \leq N/f \leq 2$ , PV modes dominated and inertial-gravity waves were insignificant. Lastly, for  $N/f \ll 1/2$  it was suggested, but not demonstrated, that flow would be dominated by large-scale cyclonic vortices as in the unstratified rapidly rotating cases. Experiments exploring grid turbulence in a rotating stratified tank were carried out by Praud, Sommeria & Fincham (2006). For large magnitudes of  $Ro$ , a significant decay of kinetic energy was observed with respect to the lower- $Ro$  cases, irrespective of the stratification strength. In the low- $Ro$  regime, the intense vortices were all cyclonic. At late times, they took the form of lens-like eddies with an aspect ratio proportional to  $f/N$ .

The final state of an initially inertially unstable distribution of vorticity is of interest. Kloosterziel, Carnevale & Orlandi (2007a) studied the unfolding of the inertial instability in initially barotropic vortices in a uniformly stratified fluid. The simulations were axisymmetric such that the effects of inertial instability were isolated. Barotropic vortex dipoles emerged, mixing momentum such that flow evolved to a state that was no longer inertially unstable. A theoretical construction was also provided to infer the final state of angular momentum at high Reynolds number given the initial distribution. Interestingly, the arguments of Kloosterziel *et al.* (2007a) implied that the inertial instability would mix the rotating shear layer to a state with nearly zero absolute vorticity as was indeed found by Métais *et al.* (1995), Kloosterziel, Orlandi & Carnevale (2007b) and Plougonven & Zeitlin (2009) through DNS of anticyclonic cases with weak system rotation rate. Carnevale *et al.* (2011) provided a method to predict the aftermath of vortex breakup in unstratified rotating flow taking into account both inertial and barotropic instability of vortices.

Observations of asymmetry between cyclonic and anticyclonic vortices in nature as well as in laboratory/numerical experiments have prompted stability analyses of barotropic vortices under the influence of stratification and rotation. Potylitsin & Peltier (1998) explored the effect of stratification and rotation on the three-dimensional stability of barotropic vortices with elliptic cross-sections resulting from the KH instability of a hyperbolic-tangent shear layer. Maximum destabilization in the unstratified case was observed for anticyclonic rotation with  $Ro^{-1} = -\Omega/S = -0.2$ , with the edge-mode growth rate being dominant, and the inertial instability mechanism underlying this instability being absent in the non-rotating case. Stratification was found to suppress the stationary edge mode, while only slightly attenuating the first-harmonic edge mode. No additional modes were found to emerge in the presence of

stratification. The elliptical mode is least influenced by stratification and is largely dominant for stronger anticyclonic rotation,  $-0.5 < -\Omega/S < -0.3$ . No modes were significantly unstable for  $|Ro^{-1}| \geq 0.5$ , but the stability of this regime was not explored for  $Fr^{-2} = N^2/S^2 > 0.2$ . The effect of ellipticity on three-dimensional instabilities of Stuart vortices was explored in Potylitsin & Peltier (1999). For low ellipticity the inertial instability dominated, while for high ellipticity a rotation-augmented elliptical instability was most unstable. The nonlinear evolution of columnar vortices subject to rotational effects alone was explored in Potylitsin & Peltier (2003). Here, the distinctions between nonlinear inertial and elliptical instabilities are clearly presented using isosurfaces of perturbation vorticity.

The zigzag instability of a counter-rotating vertical vortex pair in a stratified fluid introduced by Billant & Chomaz (2000) was explored by Otheguy, Billant & Chomaz (2006a) for a co-rotating vortex pair, such as emerge in a shear layer. Perturbations changed from antisymmetric to symmetric when vortices were co-rotating, and their wavelength depended on the separation distance rather than vortex radius as was the case for counter-rotating vortices. The effect of planetary rotation on the co-rotating zigzag instability was investigated by Otheguy, Billant & Chomaz (2006b). Anticyclonic rotation with  $Ro < -3.67$  was found to decrease the vertical length scale associated with zigzag instability, while weaker anticyclonic rotation rates increased the length scale. For  $Ro \rightarrow 0$ , the quasi-geostrophic scaling of vertical length scale proportional to vortex spacing multiplied by  $f/N$  was observed.

In the present paper, we follow up the linear stability analysis for a horizontally oriented rotating and stratified shear layer from Part 1 with a DNS study that includes a series of simulations with nearly 1 billion points simulating a shear layer with an initial Reynolds number of 2400. Section 2 introduces and motivates the mathematical model and simulation parameter regime. The overall evolution of the mean flow is summarized in § 3 and the approach towards a final state of zero absolute vorticity is assessed for anticyclonic rotation. The preceding literature survey shows that rotation influences the emergence of various instabilities including the inertial instability, barotropic shear instability, zigzag instability and the buoyancy-induced instability at zero absolute vorticity found in Part 1. The manifestation of these instabilities in coherent vortex dynamics is discussed in § 4 and the qualitative differences in the cases with moderate anticyclonic rotation rates are highlighted. Visualizations of vorticity are presented in § 5 to illustrate how the vortical signature of the inertial instability differs from that of the buoyancy instability which occurs when the flow passes through zero absolute vorticity. Section 6 explores the fluctuating enstrophy budget terms, paying particular attention to nonlinear vortex stretching and changes in the baroclinic torque when centreline absolute vorticity is nearly zero. In § 7, statistics to quantify the turbulent nature of fluctuations such as buoyancy Reynolds number, skewness of velocity derivative, spectra, and mixing efficiency are discussed. Conclusions are drawn in § 8.

## 2. Formulation

The dimensional equations for conservation of mass, momentum, and density for a Boussinesq fluid in a frame of reference rotating about the vertical axis are given below with dimensional variables denoted by \* (centrifugal acceleration is neglected):

$$\frac{\partial u_i^*}{\partial x_i^*} = 0, \tag{2.1}$$

$$\frac{\partial u_i^*}{\partial t^*} + \frac{\partial(u_i^* u_j^*)}{\partial x_j^*} + \epsilon_{i3k} 2\Omega^* u_k^* = -\frac{1}{\rho_0^*} \frac{\partial p^*}{\partial x_i^*} - g^* \delta_{i3} + v^* \frac{\partial^2 u_i^*}{\partial x_j^* \partial x_j^*}, \tag{2.2}$$

$$\frac{\partial \rho^*}{\partial t^*} + \frac{\partial(\rho^* u_j^*)}{\partial x_j^*} = \kappa^* \frac{\partial^2 \rho^*}{\partial x_j^* \partial x_j^*}, \tag{2.3}$$

where  $\epsilon$  is the permutation tensor. The density and pressure fields are decomposed in the following manner:

$$\rho^*(x_i^*, t^*) = \rho_0^* + \bar{\rho}^*(x_3^*) + \rho'^*(x_i^*, t^*), \tag{2.4a}$$

$$p^*(x_i^*, t^*) = \bar{p}^*(x_2^*, x_3^*) + p'^*(x_i^*, t^*), \tag{2.4b}$$

where  $\bar{\rho}^*$  represents the linear background stratification and  $\bar{p}^*$  is in hydrostatic and geostrophic balance with the initial density profile ( $\rho_0^* + \bar{\rho}^*$ ) and initial mean velocity profile. The initial mean velocity corresponds to a barotropic hyperbolic-tangent mixing layer of the form

$$\langle u_1^* \rangle = \frac{\Delta U^*}{2} \tanh\left(\frac{2x_2^*}{\delta_{\omega,0}^*}\right), \tag{2.5}$$

with linear vertical stratification  $d\langle \rho^* \rangle / dx_3^*$ , Coriolis parameter  $f^* = 2\Omega^*$ , initial vorticity thickness  $\delta_{\omega,0}^*$ , and velocity difference  $\Delta U^*$  as introduced in figure 1.

The non-dimensional variables for this problem are given as

$$t = \frac{t^* \Delta U^*}{\delta_{\omega,0}^*}, \quad x_i = \frac{x_i^*}{\delta_{\omega,0}^*}, \quad u_i = \frac{u_i^*}{\Delta U^*}, \quad \rho' = \frac{-\rho'^*}{\delta_{\omega,0}^* (d\bar{\rho}^* / dx_3^*)}, \quad p' = \frac{p'^*}{\rho_0^* \Delta U^{*2}}. \tag{2.6}$$

The following non-dimensional equations for continuity, momentum conservation, and density are obtained along with relevant non-dimensional parameters:

$$\frac{\partial u_i}{\partial x_i} = 0, \tag{2.7}$$

$$\frac{\partial u_i}{\partial t} + \frac{\partial(u_i u_j)}{\partial x_j} + \epsilon_{i3k} 2\Omega u_k = -\frac{\partial p'}{\partial x_i} + \frac{1}{Re_0} \frac{\partial^2 u_i}{\partial x_j \partial x_j} - Ri_{b,0} \rho' \delta_{i3}, \tag{2.8}$$

$$\frac{\partial \rho'}{\partial t} + \frac{\partial(\rho' u_j)}{\partial x_j} - u_3 = \frac{1}{Re_0 Pr} \frac{\partial^2 \rho'}{\partial x_j \partial x_j}, \tag{2.9}$$

$$\left. \begin{aligned} Re_0 &= \frac{\Delta U^* \delta_{\omega,0}^*}{\nu^*}, & Ri_{b,0} &= -\frac{g^* d\bar{\rho}^*}{\rho_0^* dx_3^*} \frac{\delta_{\omega,0}^{*2}}{\Delta U^{*2}} \approx \frac{N^{*2}}{S^{*2}}, \\ 2\Omega_0 &= Ro_0^{-1} = -\frac{2\Omega^* \delta_{\omega,0}^*}{\Delta U^*}, & Pr &= \frac{\nu^*}{\kappa^*}. \end{aligned} \right\} \tag{2.10}$$

Here, Prandtl number  $Pr$  is taken to be unity for the sake of reasonable computational cost.  $2\Omega$  is defined such that positive (negative) values imply cyclonic (anticyclonic) rotation; note that this convention differs from Part 1. Dirichlet boundary conditions are enforced for all flow variables at the transverse boundaries where flow variables are set to zero except for streamwise velocity  $u_1$  which takes the value associated with the mean velocity of the shear layer. Periodicity is enforced in the streamwise and vertical directions through Fourier collocation. Boundary influence increases with time as the shear layer grows laterally.

Initial conditions contain both two- and three-dimensional fluctuations. The two-dimensional fluctuations are invariant in the vertical direction, and fluctuating fields are triply periodic with a prescribed spectrum. Fluctuations are confined to the

Case	$Re_0$	$Ri_{b,0}$	$Ro_0$	$2\Omega_0$	$Pr$	$L_1$	$L_2$	$L_3$	$N_1$	$N_2$	$N_3$	$N_p$
<i>Ri1A1</i>	2400	1	-1	-1	1	100	50	50	1536	768	768	256
<i>Ri1A2</i>	2400	1	-2	-0.5	1	100	50	50	1536	768	768	256
<i>Ri1A10</i>	2400	1	-10	-0.1	1	100	50	50	1536	768	768	256
<i>Ri1N</i>	2400	1	$\infty$	0	1	100	50	50	1536	768	768	256
<i>Ri1C10</i>	2400	1	10	0.1	1	100	50	50	1536	768	768	256
<i>Ri1C2</i>	2400	1	2	0.5	1	100	50	50	1536	768	768	256
<i>Ri0A10</i>	2400	0	-10	-0.1	1	100	50	50	1536	768	768	256
<i>Ri0C10</i>	2400	0	10	0.1	1	100	50	50	1536	768	768	256
<i>Ri1A1Re600</i>	600	1	-1	-1	1	80	40	40	512	256	256	4
<i>Ri1A2Re600</i>	600	1	-2	-0.5	1	80	40	40	512	256	256	4
<i>Ri1A5Re600</i>	600	1	-5	-0.2	1	80	40	40	512	256	256	4
<i>Ri1A10Re600</i>	600	1	-10	-0.1	1	80	40	40	512	256	256	4
<i>Ri0A5Re600</i>	600	0	-5	-0.2	1	80	40	40	512	256	256	4

TABLE 1. Simulation parameters and case names. Case names begin with the initial Richardson number followed by *C*, *N*, or *A* for cyclonic, no and anticyclonic rotation, respectively. The following number is the initial Rossby number magnitude if rotation is present. Lastly, the Reynolds number is included in the label for the low-Reynolds-number simulations.  $L_i$  and  $N_i$  represent the length of domain and number of computational points, respectively, in each direction.  $N_p$  gives the number of MPI processes used for each simulation.

shear region through multiplication by a Gaussian curve. The two-dimensional fluctuations have a spectrum of the form  $E_{2D}(k) \propto k^8 \exp[-4(k/k_0)^2]$ . Three-dimensional fluctuations, on the other hand, have a shallower spectrum of the form  $E_{3D}(k) \propto k^4 \exp[-2(k/k_0)^2]$ . The two-dimensional fluctuations are approximately 20 times more energetic than the three-dimensional fluctuations and  $k_0 = \pi$ . After initialization,  $\langle u'_i u'_i \rangle = 0.021$  at the centreline.

### 2.1. Computational method

The numerical algorithm is different from Arobone & Sarkar (2010) which employed Fourier collocation in the streamwise and vertical directions and second-order staggered finite differencing in the transverse direction. Here, instead, fourth-order compact differencing on a collocated grid is performed in the transverse direction. The following details are the same as in Arobone & Sarkar (2010) and included for completeness. The Navier–Stokes and density equations are marched using a third-order Runge–Kutta time scheme. A Rayleigh damping function is used near the  $x_2 = \pm L_2/2$  boundaries, with a width of approximately  $3\delta_{\omega,0}$ , to prevent spurious reflections. The Poisson equations for pressure and removal of velocity divergence are solved using the Thomas algorithm. Parallelization is accomplished using message passing interface. Case-specific computational details are shown in table 1.

### 2.2. Case study

A total of eight computationally intensive simulations at  $Re_0 = 2400$  were performed as listed in table 1. Six simulations included stable stratification, while the other two were effectively unstratified with a vertical density gradient but no gravitational force. Three anticyclonic rotation rates were explored in the stratified cases, while one was explored in the unstratified cases. The *Ri1A10*, *Ri1A2*, and *Ri1A1* cases

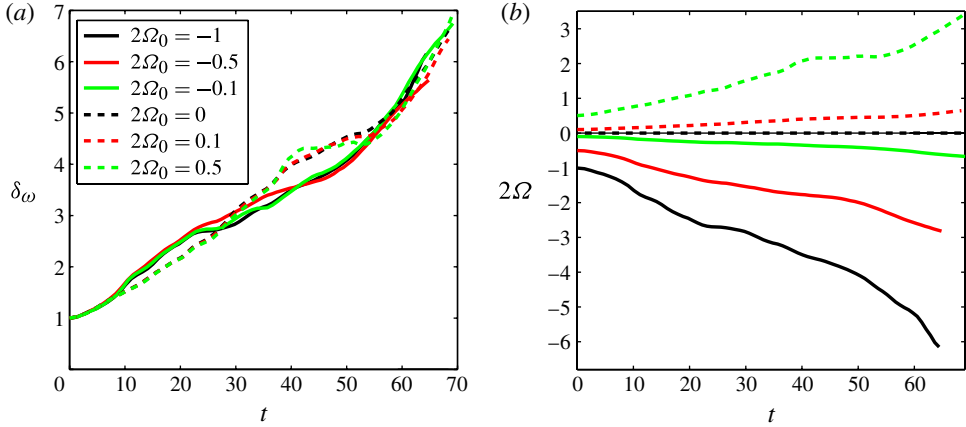


FIGURE 3. (Colour online) Temporal evolution of (a) vorticity thickness  $\delta_\omega$  and (b) non-dimensional rotation rate  $2\Omega(t) = 2\Omega^*\delta_\omega(t)/\Delta U$  for each stratified case at  $Re_0 = 2400$ . Note that positive (negative)  $\Omega_0$  corresponds to cyclonic (anticyclonic) rotation.

explore the inertially unstable regime and zero absolute vorticity state, with *RiA10* running entirely in the inertially unstable regime, *RiA1* starting with zero absolute vorticity, and *RiA2* passing through both inertially unstable and the zero absolute vorticity states. The selection of  $Ri_{b,0} = 1$  for the stratified cases is motivated by the observation of statistics showing a strong dependence on  $Ri_b(t)$  for  $Ri_b(t) \gtrsim 1$  and self-similar statistical behaviour for  $Ri_b(t) \gtrsim 10$  in Arobone & Sarkar (2010). The value of  $Ri_b(t)$  increases by a factor of nearly 50 in our simulations owing to the roughly sevenfold increase in shear layer thickness. Therefore the choice of initial stratification corresponding to  $Ri_{b,0} = 1$  is likely to be sufficient to explore the strongly stratified regime. Approximately 1 billion points are employed for the  $Re_0 = 2400$  cases leading to excellent resolution with at least 5 decades drop in energy spectra during the evolution of the flow. Five smaller simulations with one third as many grid points in each direction were also performed at lower Reynolds number. These cases are used to aid in understanding the far more complex higher- $Re$  simulations.

### 3. Overall evolution of the mean flow

Figure 3(a) shows that the shear layer width, measured by the vorticity thickness, grows with increasing time. The difference of shear layer width among the various cases is not large but, as will be shown later in detail, the evolution of the fluctuations differs qualitatively in many aspects. Figure 3(b) shows that the magnitude of non-dimensional rotation rate,  $2\Omega(t) = 2\Omega^*\delta_\omega(t)/\Delta U^*$ , increases with time since  $\delta_\omega(t)$  increases. Thus, rotation exerts increasing control during the course of the simulations. The stratified case with  $2\Omega_0 = -0.5$  exhibits a reduction of growth rate at intermediate time, passes through the zero absolute vorticity state, and continues to thicken. Figure 4 shows the evolution of mean velocity in the shear layer for low- $Re$  cases with  $2\Omega_0 = -0.2$  without and with stratification. Figure 4(a) shows that the mean flow in the case without stratification evolves to a quasi-steady state; this state corresponds to  $\langle \omega_3 \rangle + 2\Omega_0 \approx -0.04$ . The results are consistent with the mixing of angular momentum to a zero absolute vorticity state found by Métais *et al.* (1995) and suggested by Kloosterziel *et al.* (2007b) to be the high- $Re$  limit of inertially

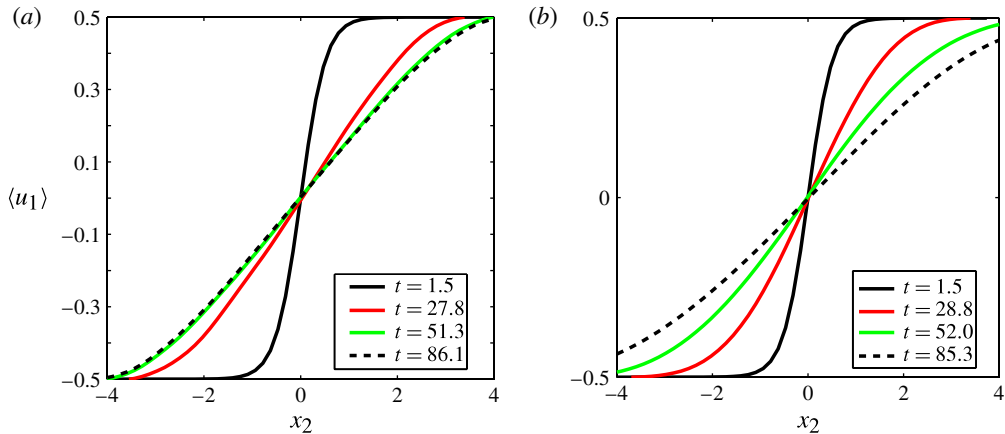


FIGURE 4. (Colour online) The temporal evolution of the mean flow in the shear layer (a) without and (b) with stratification for cases with  $Re_0 = 600$  and with weak anticyclonic rotation,  $2\Omega_0 = -0.2$ . (a)  $Ri_{b,0} = 0$ , case  $Ri0A5Re600$ ; (b)  $Ri_{b,0} = 1$ , case  $Ri1A5Re600$ .

unstable flows. Correspondingly, the vorticity thickness stops increasing at late time. In the stratified  $2\Omega_0 = -0.2$  case of figure 4(b), the flow does not become quasi-steady. The value of  $\delta_\omega$  shows a slight plateau near zero absolute vorticity, but then exhibits unabated increase.

The reasons for the stratified flow to continue mixing momentum beyond the zero mean value of absolute vorticity,  $\omega_a = \omega_3 + 2\Omega_0$ , are examined. An evolution equation for mean absolute vertical enstrophy,  $\langle \omega_a \rangle^2/2$ , is

$$\overbrace{\frac{\partial}{\partial t} \left[ \frac{1}{2} \langle \omega_a \rangle^2 \right]}^{\text{DDT}} = \overbrace{\langle u'_2 \omega'_3 \rangle \frac{\partial \langle \omega_a \rangle}{\partial x_2}}^{\text{PROD}} - \frac{\partial}{\partial x_2} [\langle \omega_a \rangle \langle u'_2 \omega'_3 \rangle] + \overbrace{\langle \omega_a \rangle \langle \omega'_k s'_{k3} \rangle}_{\text{VS\_MV}} + \overbrace{\frac{1}{Re} \langle \omega_a \rangle \frac{\partial^2 \langle \omega_a \rangle}{\partial x_2 \partial x_2}}^{\text{DISS}}, \quad (3.1)$$

and its domain-integrated terms are plotted in figure 5. Mean absolute enstrophy is analysed as opposed to mean relative enstrophy,  $\langle \omega_3 \rangle^2/2$ , due to the latter's explicit dependence on rotation rate. The nonlinear stretching and tilting term, VS\_MV, is also present in the equation for fluctuating vertical enstrophy,  $\langle \omega_3^2 \rangle/2$ , evolving differently between stratified and unstratified cases. In strongly turbulent flows, this term is a source of both mean and fluctuating enstrophy, but in the presence of strong stratification  $\langle \omega'_k s'_{k3} \rangle$  is significantly suppressed as the flow becomes quasi-two-dimensional. The PROD term is an exchange between mean and fluctuating components of vertical enstrophy. Figure 5(a) shows that, in the unstratified case, an approximate balance between increase of  $\langle \omega_a \rangle^2$  by VS\_MV and reduction by PROD is found for  $t > 50$  leading to an asymptotic state with DDT approximately zero. Quasi-two-dimensional flow also acts to increase the magnitude of PROD through enhanced lateral stirring of vertical vorticity. Additionally, the zero absolute vorticity instability of Part 1 only emerges in the presence of strong stratification and may be responsible for the increase in magnitude of PROD when  $t \approx 55$  in figure 5(b). It is worth nothing that  $2\Omega(t = 55) = -1.09$  and the centreline absolute vorticity is zero when  $t \approx 46$ . As will be shown in § 6, the baroclinic production of lateral vorticity ( $\omega_2$ ) helps maintain fluctuating enstrophy beyond the zero absolute vorticity state.

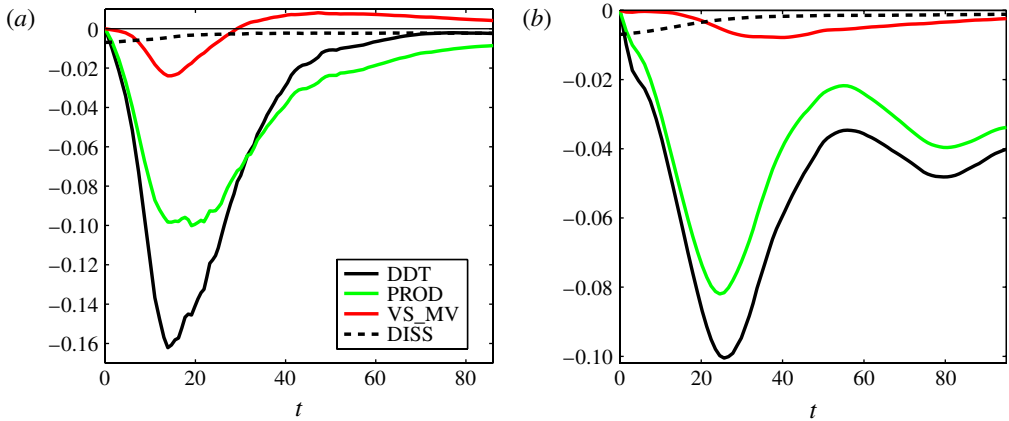


FIGURE 5. (Colour online) The temporal evolution of integrated enstrophy budget terms (a) without and (b) with stratification for cases with  $Re_0 = 600$  and with weak anticyclonic rotation,  $2\Omega_0 = -0.2$ . The terms have been scaled by  $\delta_\omega^2(t)$  adjusting for variation due to lateral spreading of enstrophy: (a)  $Ri_{b,0} = 0$ , case  $Ri0A5Re600$ ; (b)  $Ri_{b,0} = 1$ , case  $Ri1A5Re600$ .

#### 4. Dynamics of coherent structures

Coherent vortical structures are isolated using the  $\lambda_2$  criterion of Jeong & Hussain (1995), defined as the median eigenvalue of the symmetric tensor  $S_{ik}S_{kj} + \Omega_{ik}\Omega_{kj}$ .  $S_{ij}$  and  $\Omega_{ij}$  are the rate of strain and rotation tensors, respectively. Use of  $\lambda_2$  enables straightforward three-dimensional visualization of coherent vortex dynamics by rendering surfaces where  $\lambda_2 = \epsilon$ , with a small negative threshold  $\epsilon = -0.01$  as in Part 1. The authors have selected  $\lambda_2$  over  $\Delta$  or  $Q$ , which from experience generate significant false positives in the shear layer, especially in the braid region. Owing to the large size of datasets, Lagrangian methods of coherent vortex extraction are prohibitively expensive and were not employed.

##### 4.1. Non-rotating stratified case

Isocontours of  $\lambda_2$  were used by Arobone & Sarkar (2010) to explore coherent vortex dynamics in a stratified horizontal shear layer. A transition from three-dimensional incoherent turbulence to coherent quasi-vertical structures to dislocated vortex cores was observed in their strongly stratified case, A3, with  $Ri_{b,0} = 1.13$ . A mechanism qualitatively similar to the zigzag instability was found to be responsible for slicing and breaking apart these quasi-vertical coherent vortices that emerged from the soup of turbulence. Case  $A3_{low}$  of Arobone & Sarkar (2010) had very small-amplitude initial fluctuations, did not develop three-dimensional incoherent turbulence, but did result in quasi-vertical coherent vortices, the zigzag instability, and vertical slicing at late time similar to case A3. The evolution of case  $Ri1NRe600$  is similar to case  $A3_{low}$ . This is probably due to the quasi-two-dimensional initial conditions used here that favour the early formation of coherent structures as opposed to fully three-dimensional as in Arobone & Sarkar (2010). In case  $Ri1N$ , with the same stratification but higher  $Re_0 = 2400$ , coherent dynamics are quite similar with vertical length scale associated with slicing remaining unchanged, but with far greater fine-scale structure in the braid region.

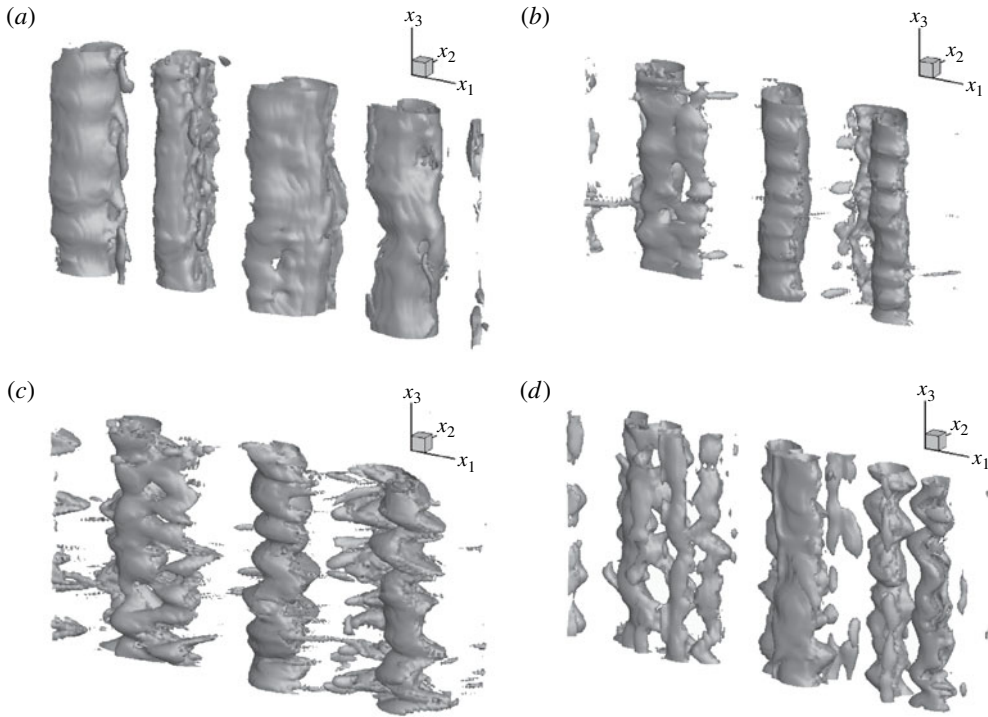


FIGURE 6. Snapshots of vertical variation showing the early-time deformation of coherent, columnar structures in the stratified non-rotating and anticyclonic rotation cases. Isosurfaces of  $\lambda_2$  for the subdomain  $x_1 \in [0, 25]$ ,  $x_2 \in [-12.5, 12.5]$ ,  $x_3 \in [0, 12.5]$ . (a) Non-rotating case *Ri1N* at  $t = 12.3$ ; (b)  $2\Omega_0 = -0.1$  case *Ri1A10* shown where  $2\Omega(t = 12.9) = -0.19$ ; (c)  $2\Omega_0 = -0.5$  case *Ri1A2* shown where  $2\Omega(t = 12.6) = -0.96$ ; (d)  $2\Omega_0 = -1$  case *Ri1A1* shown where  $2\Omega(t = 6.85) = -1.31$ .

#### 4.2. Rotating unstratified cases

Both high-*Re* unstratified simulations with weak rotation (*Ri0A10* and *Ri0C10*) exhibit a rapid transition to turbulence, with the anticyclonic case appearing considerably more unstable. The lower-*Re* unstratified cases show clearer qualitative differences between cyclonic and anticyclonic cases. The  $2\Omega_0 = -0.1$  case begins with quasi-vertical vortical structures, which shed coherent longitudinal structures until being completely destroyed by turbulent fluctuations. For  $2\Omega_0 = -0.2$ , the quasi-vertical vortices are almost immediately pinched off forming longitudinal structures, as in Métais *et al.* (1995), which then become turbulent and the flow gradually transitions into a fully turbulent state. The cyclonic  $2\Omega_0 = 0.1$  case contains quasi-vertical structures that still shed longitudinal vortices, although they are far less commonplace than in the anticyclonic cases. Most shedding and destabilization in the cyclonic case occur later during vortex merging, perhaps indicative of elliptic instability.

#### 4.3. Anticyclonic rotation with stratification

The coherent structures evolve differently among the stratified anticyclonic cases and even more so with respect to the non-rotating stratified case. Figure 6 shows a section of the coherent structures in four stratified cases with increasing anticyclonic rotation. In all cases, the barotropic instability develops leading to columnar vortex cores that

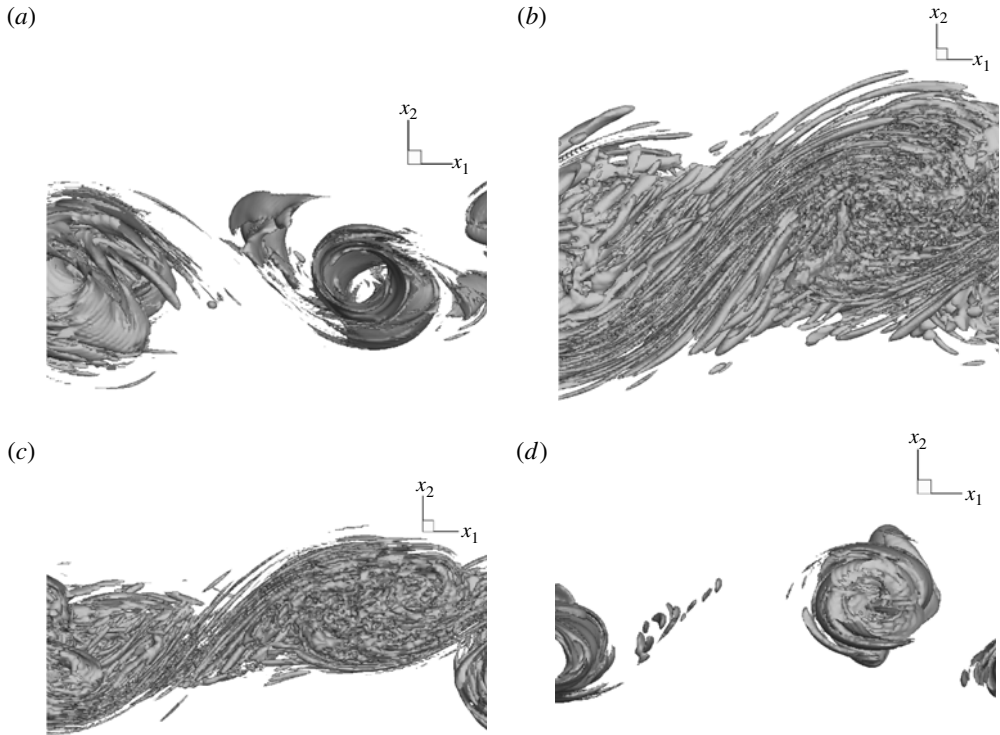


FIGURE 7. Snapshots of horizontal variation at late time. A network of longitudinal braid vortices is seen only in the stratified cases with moderate anticyclonic rotation, irrespective of  $Re_0$ . Isosurfaces of  $\lambda_2$  for the subdomain  $x_1 \in [0, 25]$ ,  $x_2 \in [-12.5, 12.5]$ ,  $x_3 \in [0, 12.5]$  show the final coherent structures viewed in the negative  $x_3$  direction. (a) Non-rotating case  $Ri1N$  at  $t = 68.9$ ; (b)  $2\Omega_0 = -0.1$  case  $Ri1A10$  shown where  $2\Omega(t = 69.2) = -0.67$ ; (c)  $2\Omega_0 = -0.5$  case  $Ri1A2$  shown where  $2\Omega(t = 64.8) = -2.82$ ; (d)  $2\Omega_0 = -1$  case  $Ri1A1$  shown where  $2\Omega(t = 65.2) = -6.28$ .

subsequently deform. While figure 6(a–c) contains snapshots from roughly the same time into the simulation, figure 6(d) is a much earlier snapshot due to the more rapid deformation of the barotropic modes in the  $2\Omega_0 = -1$  case. The fact that the initial deformation is largest in the  $2\Omega_0 = -1$  case points to the importance of the *zero-absolute vorticity instability* identified in Part 1. Figures 7 and 8 show coherent structures via horizontal and vertical snapshots, respectively, from the end of each simulation whose early-time structures were presented in figure 6.

For  $Ri1A10$ , quasi-vertical structures form and quickly develop high-vertical-wavenumber deformations ( $k_3 \approx 2.75$ ) as seen in figure 6(b). The corrugated edges of the vortices, the so-called rib vortices of Kloosterziel *et al.* (2007a), interact with nearby vortex cores and are then shed off as coherent braid structures that surround the quasi-vertical modes. The network of braid vortices grows throughout the remainder of the simulation, obfuscating extraction of the behaviour underneath from the  $\lambda_2$  visualizations. Figure 7(b) is a horizontal snapshot that reveals fine-scale behaviour throughout the coherent structures. In the lower-Reynolds-number case,  $Ri1A10Re600$ , deformations of the vortex cores are also observed with a similar wavenumber ( $k_3 \approx 2.67$ ), but coherent braid structures do not emerge after the vortex edges are

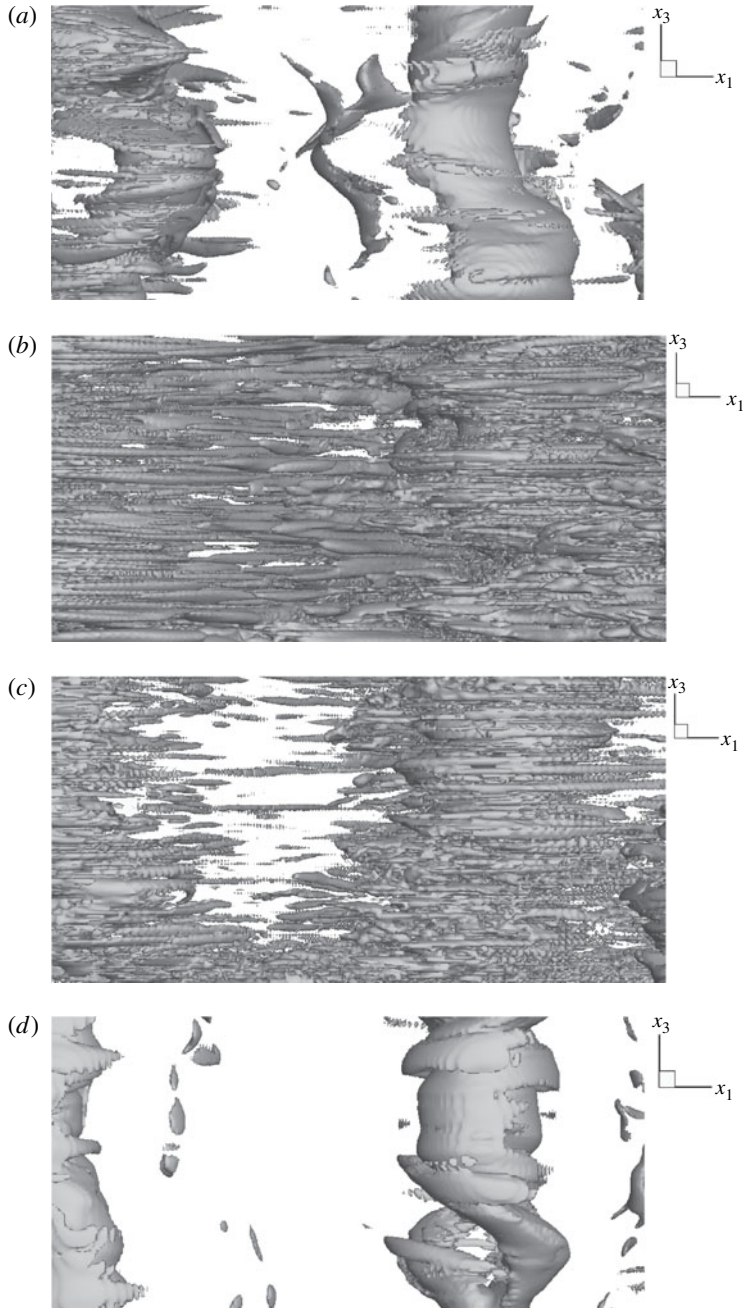


FIGURE 8. Isosurfaces of  $\lambda_2$  for the subdomain  $x_1 \in [0, 25]$ ,  $x_2 \in [-12.5, 12.5]$ ,  $x_3 \in [0, 12.5]$  showing coherent structures in the stratified cases viewed in the positive  $x_2$  direction. (a) Non-rotating case *Ri1N* at  $t = 68.9$ ; (b)  $2\Omega_0 = -0.1$  case *Ri1A10* shown where  $2\Omega(t = 69.2) = -0.67$ ; (c)  $2\Omega_0 = -0.5$  case *Ri1A2* shown where  $2\Omega(t = 64.8) = -2.82$ ; (d)  $2\Omega_0 = -1$  case *Ri1A1* shown where  $2\Omega(t = 65.2) = -6.28$ .

shed. It is important to note that the  $k_1 = 0.44$  (dominant KH wavelength) inertial mode is not excited until  $2\Omega(t) \approx -0.2$ . This may explain the low deformation of the vortices in figure 6(b) compared to 6(c) and 6(d) which have more rapid rotation rates. The range of unstable  $k_1$  values increases as the anticyclonic rotation rate increases as shown in figure 3(b,e) from Part 1. Even though the  $k_1 = 0$  mode is unstable for  $-1 < 2\Omega < 0$ , higher streamwise wavenumbers (in the shear layer high- $k_1$  modes arise owing to the initial barotropic instability or later vortex interactions) require more rapid rotation for vertical destabilization.

The *Ri1A2* case exhibits deformations in the quasi-vertical vortices, with a higher wavenumber ( $k_3 \approx 4$ ). These deformations distort the quasi-vertical modes more than in the weaker anticyclonic rotation case, especially near the zero absolute vorticity state, after which incoherent vorticity fluctuations appear around the ‘zigzagging’ vortex modes. Figure 6(c) shows the *Ri1A2* case shortly before the zero absolute vorticity state, when  $2\Omega(t) = -0.96$ . Interestingly, coherent longitudinal braid structures emerge in case *Ri1A2* shortly later, although not nearly as intensely as in *Ri1A10*, even though  $2\Omega(t) < -1$  signifying that the flow is globally inertially stable. This is surprising given the fact that these structures have been traditionally associated with the inertial instability (Métais *et al.* 1995; Kloosterziel *et al.* 2007a). Case *Ri1A2Re600* shows similar behaviour to the higher-*Re* case at early time, but incoherent fluctuations are less prevalent and the flow is quickly stabilized without the formation of coherent braid vortices. The resulting network of vortices interact minimally except when the separation distance is small enough that local shear is of comparable order to the coordinate system rotation rate.

High-vertical-wavenumber ( $k_3 \approx 2.5$ ) deformations are also observed earlier in the *Ri1A1* case (figure 6d), which deform the quasi-vertical modes quickly compared to the weaker anticyclonic cases. No significant small-scale incoherent structure emerges and vortex evolution is similar to that of *Ri1A2Re600* at late time, where vortices advect passively and only interact significantly once they are in very close proximity with one another. The qualitative similarities between cases *Ri1A1* (high rotation and high *Re*) and *Ri1A2Re600* (moderate rotation and low *Re*) are likely to be due to the fact that the increased destabilization due to moderate rotation in case *Ri1A2Re600* is nearly offset by the increased stabilization of viscosity. At higher initial rotation,  $2\Omega_0 = -1$ , the coherent vortex cores in the lower-*Re* case, *Ri1A1Re600*, evolved similarly to those at higher *Re* except with smoother vorticity isocontours and less small-scale content.

The structures tend to deform in the  $x_1$ - $x_3$  plane near the zero absolute vorticity state,  $2\Omega(t) = -1$ , for both *Ri1A2* and *Ri1A1*. This corresponds to formation of small-scale  $\omega'_2$ , consistent with the linearized inviscid evolution equations at the centreline for the zero absolute vorticity state, given in equation (5.2) of Part 1:

$$\frac{\partial \omega'_1}{\partial t} = \left( \frac{\langle s_{12} \rangle}{2} + \Omega_0 \right) \omega'_2 - Ri_{b,0} \frac{\partial \rho'}{\partial x_2}, \quad \frac{\partial \omega'_2}{\partial t} = Ri_{b,0} \frac{\partial \rho'}{\partial x_1}. \quad (4.1)$$

Streamwise density gradients efficiently generate  $\omega'_2$  near this state due to the lack of influence of mean shear on the evolution equation for lateral vorticity fluctuations. Alternating filaments of  $\omega'_2$  surround the columnar vortices and shear them rather quickly.

Vertical sections at later times show that coherent structures in the weakly and moderate anticyclonic cases *Ri1A10* and *Ri1A2* evolve quite differently from one another, but with a few key similarities. Both cases result in a network of thin coherent longitudinal vortices as seen in figure 8(b,c), with the network being more prevalent

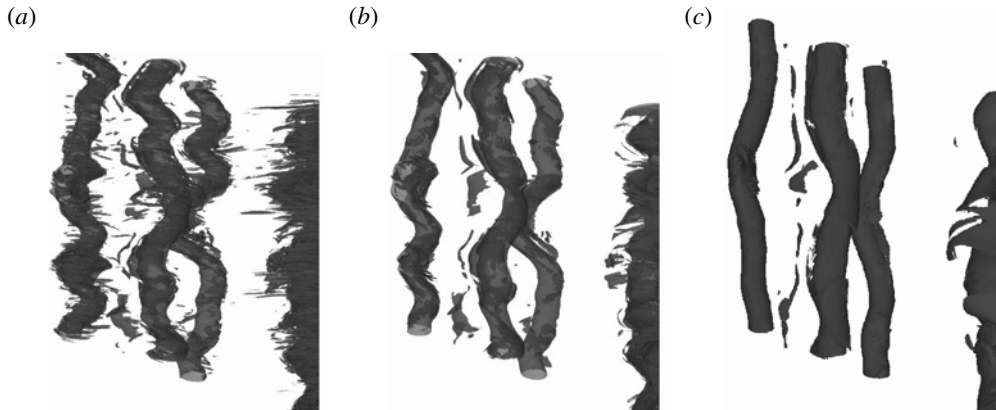


FIGURE 9. Isosurfaces of  $\lambda_2$  for the subdomain left of the  $x_2$ - $x_3$  midplane showing the effect of cyclonic rotation on coherent structures in the stratified cases: (a)  $2\Omega_0 = 0$  case *Ri1N* at  $t = 68.9$ ; (b)  $2\Omega_0 = 0.1$  case *Ri1C10* where  $2\Omega(t = 69.1) = 0.65$ ; (c)  $2\Omega_0 = 0.5$  case *Ri1C2* where  $2\Omega(t = 69.1) = 3.46$ .

in the weaker anticyclonic case with  $2\Omega_0 = -0.1$ . Initially, in both cases, vortices deform in a similar manner with a small vertical length scale. Later, however, the large quasi-vertical structures do not break apart in the weakly anticyclonic case, remaining columnar, while breaking apart in the moderate anticyclonic case with  $2\Omega_0 = -0.5$ .

#### 4.4. Cyclonic rotation with stratification

The evolution of coherent vortices is very similar for the non-rotating stratified case and the cyclonic stratified cases, and strongly contrasts with the anticyclonic cases. Vertical slicing is slightly less dramatic in the cyclonic cases than in the non-rotating case, but there is a clear one-to-one matching of vortical structures between the three cases throughout the duration of the simulations. Figure 9(a-c) illustrates these points, clearly showing coherent structures at the end of each simulation. The cleaner nature of the coherent structures in the cyclonic cases is also noteworthy.

### 5. Vortical signature of instabilities

The linear analysis of Part 1 suggests that the inertial instability and zero absolute vorticity mechanism generate horizontal vorticity fluctuations in distinct manners. Figures 10(a) and 10(b) illustrate the differences between the nonlinear evolution of the inertial instability and the zero absolute vorticity instability. Figure 10(a) contains only thin sheet-like vortex structures associated with the inertial instability, while figure 10(b) contains both thin sheet-like structures and arrays of alternating vorticity which are prevalent near the zero absolute vorticity state. The sheet-like structures take more time to induce local shear instability than the vortex arrays which quickly overturn generating small-scale vorticity.

Case *Ri1A10* experiences significant destabilization owing to the nonlinear evolution of the inertial instability as illustrated in figure 11. The inertial instability is manifested as coherent longitudinal vortices in the braid region, as seen in the previous section, and thin sheet-like vortex structures in the core region. These sheet-like vortex structures are susceptible to rolling up at later times as seen in figure 11, which shows the transition from sheet-like structures of  $\omega_2$  to KH billows in several

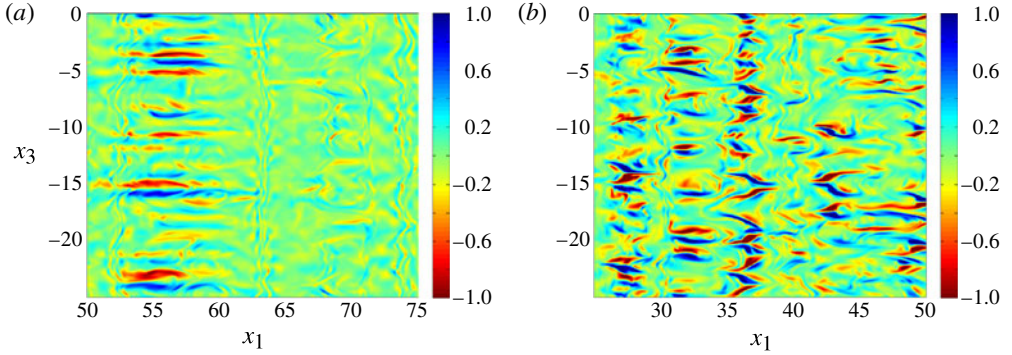


FIGURE 10. (Colour online) Laplacian filtered  $\omega_2$  fluctuations given for a segment of the  $x_1$ – $x_3$  midplane illustrating differences between instabilities in the (a) weak anticyclonic and (b) moderate anticyclonic cases: (a)  $2\Omega_0 = -0.1$  case *Ri1A10* where  $2\Omega(t = 21.89) = -0.26$ ; (b)  $2\Omega_0 = -0.5$  case *Ri1A2* where  $2\Omega(t = 13.6) = -1.01$ .

locations, which are circled. Figures 11(a) and 11(b) correspond to  $2\Omega(t) = -0.40$  and  $2\Omega(t) = -0.56$ , respectively, implying that rollup occurs near the most linearly unstable state of  $2\Omega(t) = -0.5$ .

The horizontal vorticity components show dramatic differences with respect to system rotation in the stratified simulations, and are by far the most active in the *Ri1A2* and *Ri1A10* cases. Vertical layering is most dramatic in *Ri1A2* at later times, even though the effect of rotation is stabilizing, while the vorticity fields appear most disordered in *Ri1A10*.

## 6. Fluctuating enstrophy evolution

Figure 12 shows the evolution of fluctuating enstrophy components in each of the high-*Re* stratified cases. When  $2\Omega_0 = 0.1, 0.5$  and  $-1$ , enstrophy is primarily vertical, while horizontal enstrophy dominates for  $2\Omega_0 = -0.1$  and  $-0.5$ . In order to quantify the processes responsible for modifying enstrophy components, fluctuating enstrophy budgets are computed. Equations are derived for the evolution of  $x_1$ – $x_3$  plane-averaged fluctuating enstrophy components and given below for the horizontal shear layer (no summation over Greek indices):

$$\begin{aligned} \frac{\partial \langle \omega'_\alpha \omega'_\alpha \rangle}{\partial t} = & -2 \langle \omega'_\alpha u'_2 \rangle \frac{\partial \langle \omega_\alpha \rangle}{\partial x_2} - \frac{\partial \langle \omega'_\alpha \omega'_\alpha u'_2 \rangle}{\partial x_2} + 2(\langle \omega_3 \rangle + 2\Omega_0) \langle \omega'_\alpha s'_{\alpha 3} \rangle \\ & + 2 \langle \omega'_\alpha \omega'_j \rangle \langle s_{\alpha j} \rangle + 2 \langle \omega'_\alpha \omega'_j s'_{\alpha j} \rangle + \epsilon_{\alpha j 3} 2\Omega_0 \langle \omega'_\alpha \omega'_j \rangle + \frac{1}{Re_0} \frac{\partial^2 \langle \omega'_\alpha \omega'_\alpha \rangle}{\partial x_j \partial x_j} \\ & - \frac{2}{Re_0} \left\langle \frac{\partial \omega'_\alpha}{\partial x_j} \frac{\partial \omega'_\alpha}{\partial x_j} \right\rangle - \epsilon_{\alpha j 3} 2Ri_{b,0} \left\langle \omega'_\alpha \frac{\partial \rho'}{\partial x_j} \right\rangle. \end{aligned} \quad (6.1)$$

The physical meaning of each term is as follows:

$$\text{rate of change of fluctuating enstrophy (DDT)} \quad \frac{\partial \langle \omega'_\alpha \omega'_\alpha \rangle}{\partial t};$$

$$\text{production of fluctuating enstrophy (PROD)} \quad -2 \langle \omega'_\alpha u'_2 \rangle \frac{\partial \langle \omega_\alpha \rangle}{\partial x_2};$$

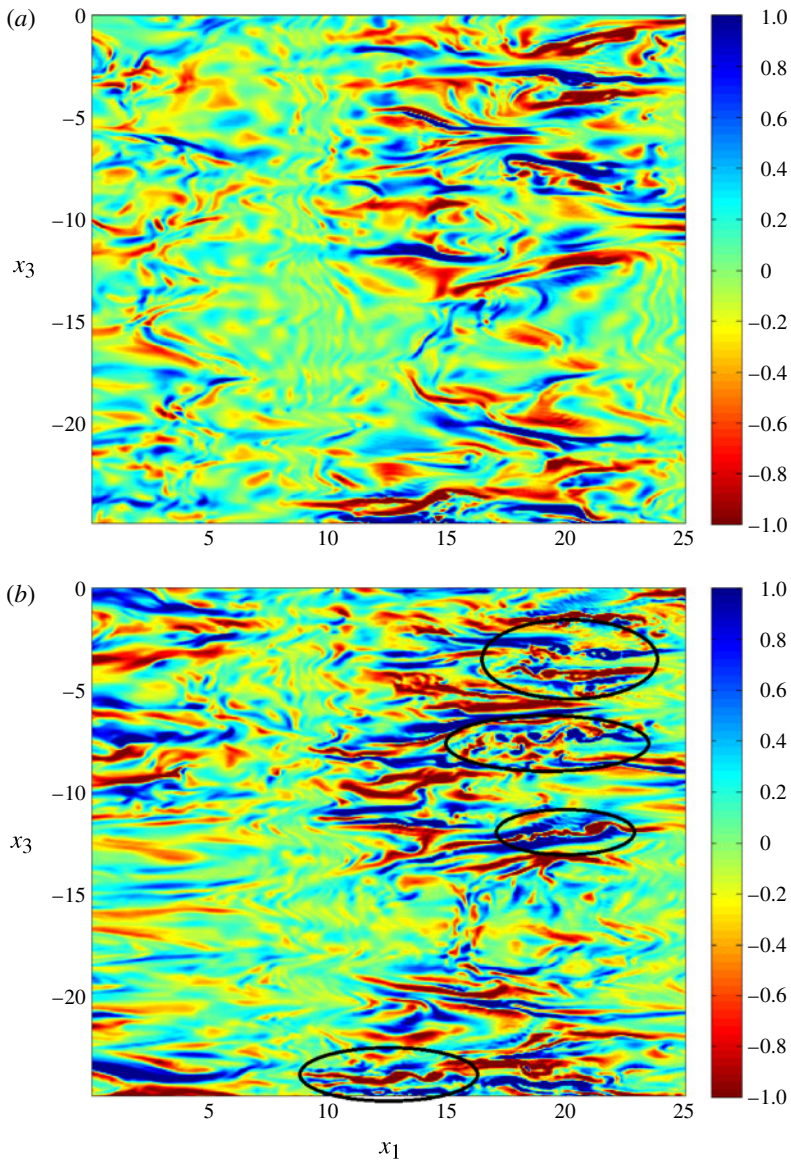


FIGURE 11. Plots of Laplacian filtered  $\omega_2$  from the *Ri1A10* case with  $2\Omega_0 = -0.1$  showing development of fine-scale KH instabilities (circled) and vortical structure as the flow passes through the most inertially unstable regime ( $2\Omega(t) = -0.5$ ): (a)  $2\Omega(t = 48.94) = -0.40$ ; (b)  $2\Omega(t = 61.22) = -0.56$ .

transport of fluctuating enstrophy by  
 velocity fluctuations (TR) 
$$-\frac{\partial \langle \omega'_\alpha \omega'_\alpha u'_2 \rangle}{\partial x_2};$$

stretching/tilting of mean absolute  
 vorticity by fluctuating strain (VS\_MV) 
$$2(\langle \omega_3 \rangle + 2\Omega_0) \langle \omega'_\alpha s'_\alpha \rangle;$$

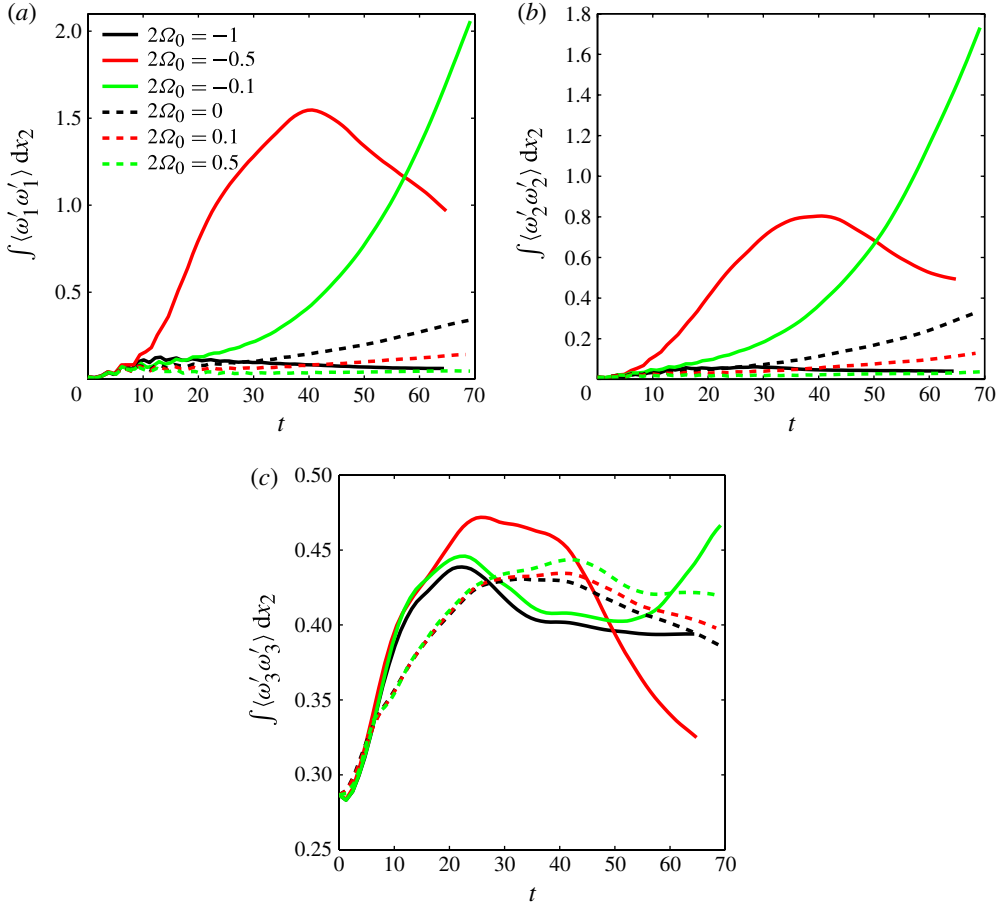


FIGURE 12. (Colour online) Temporal evolution of the three integrated enstrophy components in stratified cases where  $Ri_{b,0} = 1$  and  $Re_0 = 2400$ .

stretching/tilting of fluctuating vorticity by mean strain (VS_MS)	$2\langle \omega'_\alpha \omega'_j \rangle \langle s_{\alpha j} \rangle$ ;
stretching/tilting of fluctuating vorticity by fluctuating strain (VS_F)	$2\langle \omega'_\alpha \omega'_j s'_{\alpha j} \rangle$ ;
effect of coordinate system rotation (ROT)	$\epsilon_{\alpha j 3} 2\Omega_0 \langle \omega'_\alpha \omega'_j \rangle$ ;
viscous diffusion of enstrophy fluctuations (DIFF)	$\frac{1}{Re_0} \frac{\partial^2 \langle \omega'_\alpha \omega'_\alpha \rangle}{\partial x_j \partial x_j}$ ;
viscous dissipation of enstrophy fluctuations (DISS)	$-\frac{2}{Re_0} \left\langle \frac{\partial \omega'_\alpha}{\partial x_j} \frac{\partial \omega'_\alpha}{\partial x_j} \right\rangle$ ;
fluctuating baroclinic torque (BC)	$-\epsilon_{\alpha j 3} 2Ri_{b,0} \left\langle \omega'_\alpha \frac{\partial \rho'}{\partial x_j} \right\rangle$ .

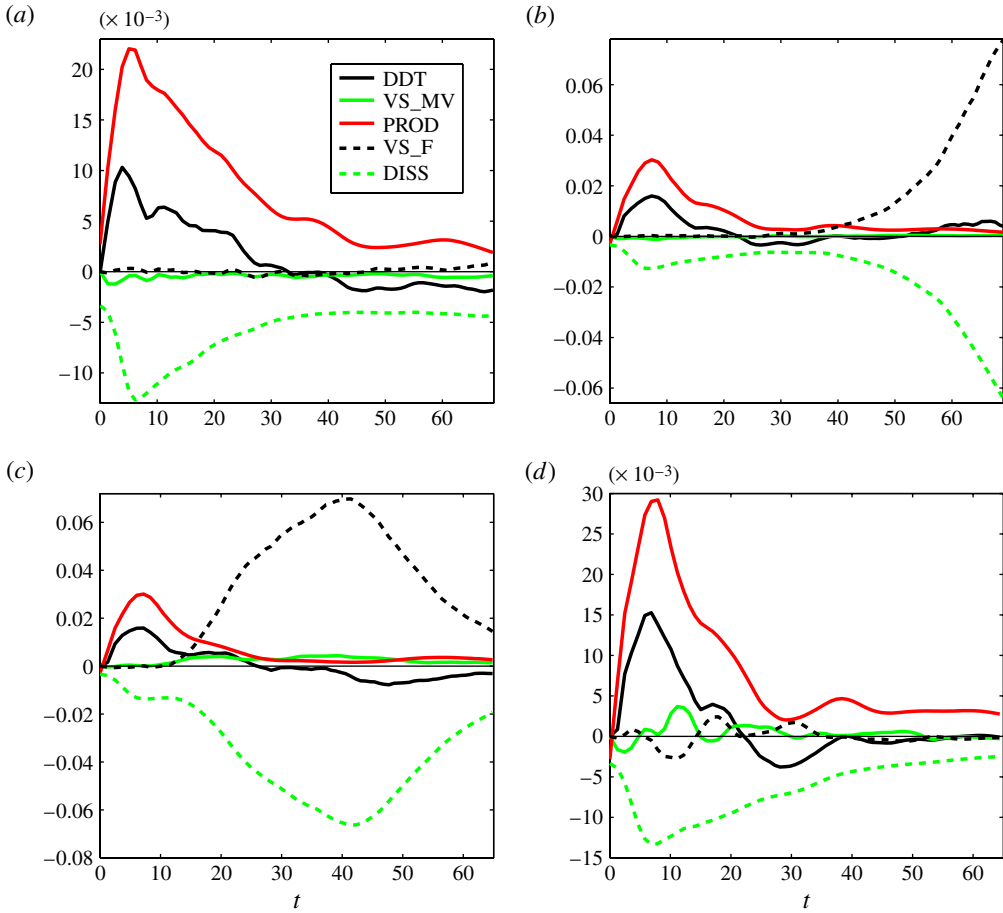


FIGURE 13. (Colour online) Temporal evolution of integrated vertical enstrophy budgets in stratified cases where  $Ri_{b,0} = 1$ . (a)  $2\Omega_0 = 0$  case  $Ri1N$ ; (b)  $2\Omega_0 = -0.1$  case  $Ri1A10$ ; (c)  $2\Omega_0 = -0.5$  case  $Ri1A2$ ; (d)  $2\Omega_0 = -1$  case  $Ri1A1$ . The  $2\Omega_0 = 0.1$  and  $0.5$  cases are very similar to (a) and not shown.

The transport of fluctuating enstrophy and viscous diffusion terms integrate over the domain to zero when there are no boundary fluxes and are not discussed. In our analysis we often combine the stretching of fluctuating vorticity by mean strain term (VS\_MS) with the coordinate system rotation term (ROT) to reduce clutter in the enstrophy component budgets. VS\_MS is a source term while ROT transfers fluctuating enstrophy between horizontal components. In some cases the nonlinear vortex stretching (VS\_F) term is merged with DISS, also to reduce clutter; this term can be thought of as the imbalance between dissipation and enstrophy transfers from larger to smaller scales. Large magnitudes of VS\_F and DISS are suggestive of strong nonlinearity, a forward enstrophy cascade, and turbulence.

Initially, we focus our attention on vertical fluctuating enstrophy budgets, which are not directly influenced by buoyancy. Vertical enstrophy budgets are plotted in figure 13 for stratified cases with  $2\Omega_0 = 0, -0.1, -0.5$  and  $-1$ . Common features are observed at late time between the  $2\Omega_0 = -1$  case and the non-rotating and cyclonic (not shown,

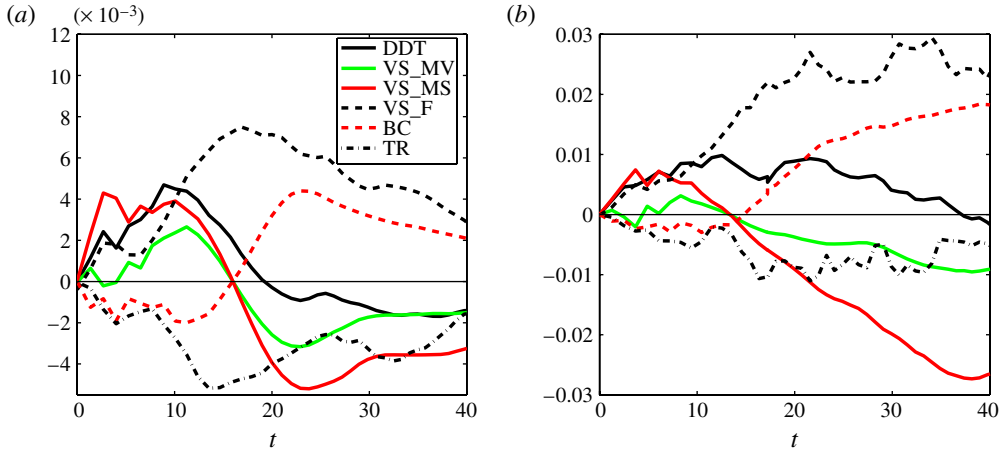


FIGURE 14. (Colour online) Temporal evolution of the  $\langle \omega'_2 \omega'_2 \rangle$  budget from the anticyclonic cases with  $2\Omega_0 = -0.5$ ,  $Ri_{b,0} = 1$ . The budget is calculated at the centreline and the plot zooms in on the early evolution. The rate of change and baroclinic torque terms are filtered to remove the influence of  $N$  oscillations. Note that  $VS\_MS = VS\_MS + ROT$  and  $VS\_F = VS\_F + DISS$  for compactness. (a)  $Re_0 = 600$  case  $Ri_{1A}2Re600$ ; (b)  $Re_0 = 2400$  case  $Ri_{1A}2$ .

but similar to non-rotating) cases. Here, the dominant balance is between PROD and DISS. This partially explains why snapshots of vertical vorticity (not shown) are significantly cleaner in these cases than in the anticyclonic cases with weaker rotation. Nonlinear stretching and tilting play a far greater role in the evolution of vertical enstrophy fluctuations in the weak and moderate anticyclonic stratified cases, even at later time when  $2\Omega(t) < -1$ . Thus, for cases  $Ri_{1A}10$  and  $Ri_{1A}2$  there are time periods when the budget is dominated by  $VS\_F$  and  $DISS$  terms, but in the  $Ri_{1A}1$ ,  $Ri_{1C}10$  and  $Ri_{1N}$  cases  $VS\_F$  never dominates.

The  $2\Omega_0 = -0.5$  case passes through  $2\Omega(t) = -1$  corresponding to zero absolute vorticity. Through figures 14–16 we demonstrate that the baroclinic term (BC) plays an important role in maintaining vorticity fluctuations beyond the zero absolute vorticity state despite the inertial stability of the flow during this stage.

Figures 14(a) and 14(b) show local lateral fluctuating enstrophy ( $\langle \omega'_2 \omega'_2 \rangle$ ) budgets from the low- and high- $Re_0$  stratified  $2\Omega_0 = -0.5$  cases at the inflection point, focusing on early time evolution. Both plots show the BC term out of phase with the linear  $VS\_MV$  and  $VS\_MS$  (actually  $VS\_MS + ROT$ ) terms, transport advecting enstrophy away from the centreline, and  $VS\_F$  (actually  $VS\_F + DISS$ ) implying a cascade of enstrophy from large scales to small. The zero absolute vorticity state is reached in the high- $Re$  case (figure 14b) when  $t \approx 13.4$ . Shortly after, when  $t \approx 14$ , baroclinic torque (BC) changes sign in the  $\langle \omega'_2 \omega'_2 \rangle$  budget, implying destabilization of lateral fluctuating enstrophy by density fluctuations. This is consistent with the dynamics of the zero absolute vorticity mode in figure 11 of Part 1, where density gradients act against  $\omega'_1$  while acting to strengthen  $\omega'_2$ . Interestingly, we see the BC,  $VS\_MV$  and  $VS\_MS$  (actually  $VS\_MS + ROT$  in figure 14) terms change signs in the local  $\langle \omega'_2 \omega'_2 \rangle$  budget at almost the same time ( $t \approx 13.4$  in figure 14b). The  $VS\_MV$  and  $VS\_MS$  ( $VS\_MS + ROT$  in figure 14) terms are exactly zero when local absolute vorticity is zero because  $\langle s_{12} \rangle - \Omega_0 = -(\langle \omega_3 \rangle + 2\Omega_0)/2 = 0$ . The DDT term of figure 14(b) shows a considerable delay in crossing the zero value relative

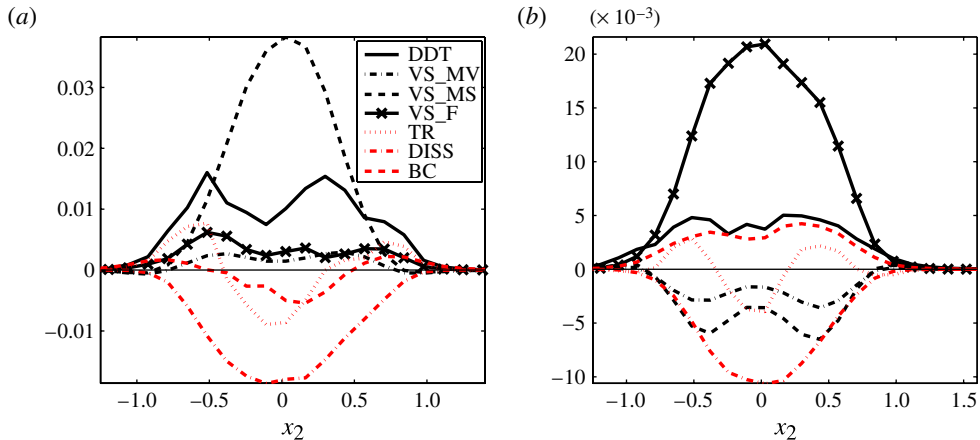


FIGURE 15. (Colour online) Enstrophy component budgets from the  $2\Omega_0 = -0.5$ ,  $Ri_{b,0} = 1$  case *Ri1A2* shown shortly after the zero absolute vorticity state. Here,  $t = 18.08$  and  $2\Omega(t) \approx -1.12$ . Note that  $VS_{MS} = VS_{MS} + ROT$  for compactness. (a)  $\langle \omega'_1 \omega'_1 \rangle$  budget; (b)  $\langle \omega'_2 \omega'_2 \rangle$  budget.

to figure 14(a), i.e. stabilization of lateral enstrophy is delayed at higher Reynolds number. Perhaps at still higher  $Re$ , destabilization could be delayed even further into the inertially stable regime.

In figures 15(a) and 15(b), lateral profiles of  $\langle \omega'_1 \omega'_1 \rangle$  and  $\langle \omega'_2 \omega'_2 \rangle$  budgets are shown for the stratified  $2\Omega_0 = -0.5$  case shortly after the zero absolute vorticity state. Although the nonlinear vortex stretching term (VS.F) is dominant in the budget for  $\langle \omega'_2 \omega'_2 \rangle$ , it is almost cancelled by the other non-baroclinic terms, particularly the dissipation. Consequently, the rate of change curve (DDT) in figure 15 for lateral fluctuating enstrophy nearly follows the baroclinic (BC) term, which was predicted by (4.1), which was derived assuming small horizontal gradients, zero absolute vorticity, and neglected nonlinearity and viscosity.

Interestingly, in figure 16(a,b), nonlinear vortex stretching and tilting are far more important in lateral enstrophy evolution than streamwise enstrophy, where stretching and tilting is nearly zero around and before the zero absolute vorticity state. For weak and moderate anticyclonic rotation rates there are times when baroclinicity is a net source of horizontal enstrophy, specifically throughout much of the  $2\Omega_0 = -0.5$  case. The DDT term in the lateral enstrophy budget in figure 16(b) suggests peak destabilization occurring in the stratified  $2\Omega_0 = -0.5$  case when  $35 \lesssim t \lesssim 40$  or  $2\Omega(t) \sim -1.75$ . In an attempt to better understand why enstrophy fluctuations grow so far into the inertially stable regime, (4.1) is manipulated to obtain the following evolution equation for fluctuating lateral enstrophy, neglecting the influence of stratification:

$$\frac{\bar{D}^2}{\bar{D}t^2} [\langle \omega'_2 \omega'_2 \rangle] = -4\Omega_0(2\Omega_0 + \langle \omega_3 \rangle) \langle \omega'_2 \omega'_2 \rangle. \quad (6.2)$$

We concentrate on fluctuating lateral enstrophy because it begins to decay before both the fluctuating streamwise enstrophy and the  $\langle \omega'_1 \omega'_2 \rangle$  correlation. Understanding the mechanism responsible for delayed decay of lateral fluctuating enstrophy may explain why dissipation and nonlinearity remain strong so long after passing through

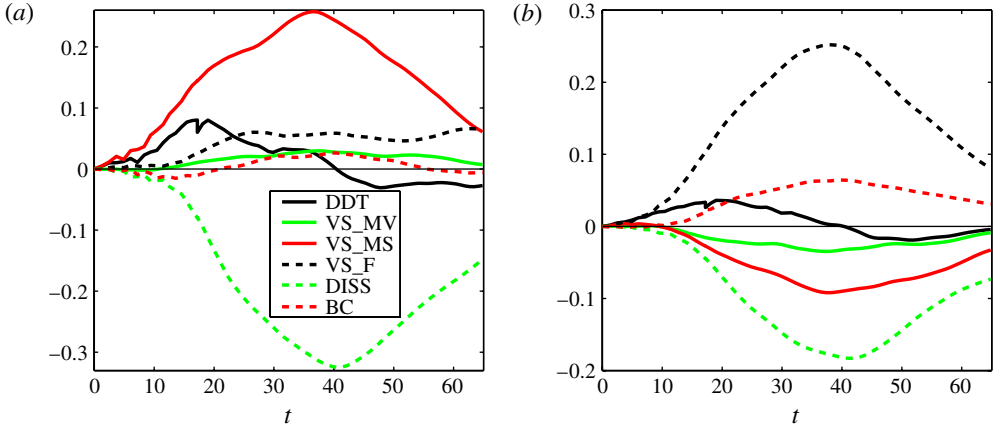


FIGURE 16. (Colour online) Temporal evolution of integrated horizontal enstrophy budgets for the moderate anticyclonic case  $Ri1A2$  with  $2\Omega_0 = -0.5$  and  $Ri_{b,0} = 1$ . The rate of change and baroclinic torque terms have been filtered to lessen the influence of  $N$  oscillations. Note that  $VS\_MS = VS\_MS + ROT$  for compactness. (a)  $\langle \omega'_1 \omega'_1 \rangle$  budget; (b)  $\langle \omega'_2 \omega'_2 \rangle$  budget.

the absolute zero vorticity state. Based on the present simulation data, mean centreline vorticity may be approximated by  $\langle \omega_3 \rangle(t) \approx (t/13 + 1)^{-1}$ , and lateral fluctuating enstrophy may be approximated as growing linearly with time. Integrating (6.2) from the beginning of the simulation until time  $t^*$  and setting the result equal to zero gives the time when  $\langle \omega'_2 \omega'_2 \rangle$  reaches peak magnitude:

$$\int_0^{t^*} 2 \left( -\frac{1}{2} + \frac{1}{t/13 + 1} \right) t dt = 0. \tag{6.3}$$

Equation (6.3) is satisfied when  $t^* \approx 21.1$ , long before the  $t^* \approx 37$  when  $\langle \omega'_2 \omega'_2 \rangle$  is found to achieve its peak in case  $Ri1A2$  as discerned by where the rate of change curve crosses the time axis in figure 14(b). Thus, destabilization continues beyond the time predicted by linear, unstratified analysis. An interesting point to note is that the baroclinic and rate of change terms in the lateral fluctuating enstrophy budget in figure 14(b) cross when  $t \approx 21$ , i.e. at this time the increase in horizontal enstrophy is entirely due to the production by baroclinicity (BC). The BC term continues to be positive and grow after  $t = 21$  while the sum of all the other terms continues to be negative and a sink. Clearly, the generation of  $\omega_2$  via baroclinic torque once  $2\Omega(t) \gtrsim -1$  helps explain the delayed stabilization of horizontal enstrophy.

### 6.1. Rapid rotation regime

Figures 17(a) and 17(b) show the streamwise and lateral fluctuating enstrophy budgets throughout the duration of case  $Ri1A1$  with initial  $2\Omega_0 = -1$ . The non-dimensional rotation rate,  $2\Omega(t)$ , increases by a factor of 7 during the simulation. Relative to the moderate rotation rate case with initial  $2\Omega_0 = -0.5$ , the terms in the enstrophy budget are smaller in this case by almost an order of magnitude. When rotation is strong ( $2|\Omega(t)| \gg 1$ ) the baroclinic terms are out of phase with the terms corresponding to stretching by mean strain and coordinate rotation. This is a consequence of flow in thermal wind (geostrophic and hydrostatic) balance, which when applied to the

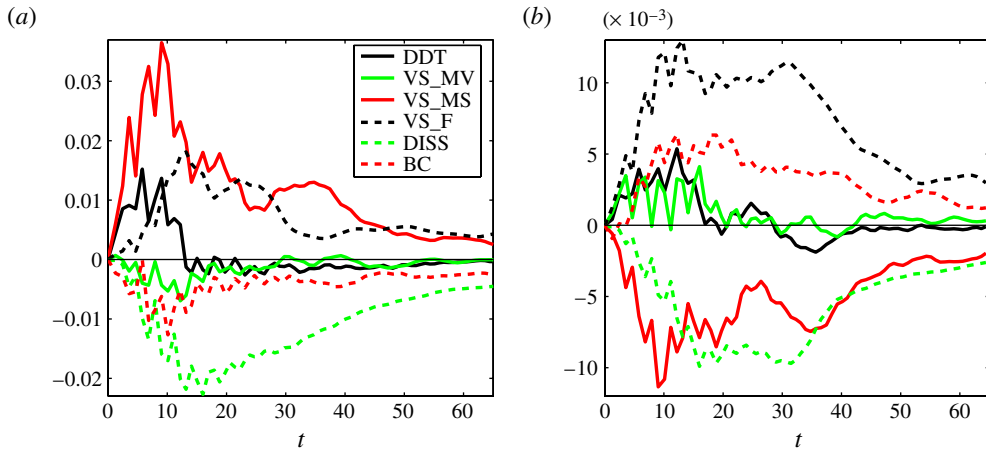


FIGURE 17. (Colour online) Temporal evolution of integrated horizontal enstrophy budgets in the rapid anticyclonic case  $Ri_{1A1}$  where  $2\Omega_0 = -1$  and  $Ri_{b,0} = 1$ . The rate of change and baroclinic torque terms have been filtered to lessen the influence of  $N$  oscillations. Note that  $VS\_MS = VS\_MS + ROT$  for compactness. (a)  $\langle \omega'_1 \omega'_1 \rangle$  budget; (b)  $\langle \omega'_2 \omega'_2 \rangle$  budget.

momentum equations gives

$$2\Omega_0 \frac{\partial u'_1}{\partial x_3} \sim Ri_{b,0} \frac{\partial \rho'}{\partial x_2}, \quad -2\Omega_0 \frac{\partial u'_2}{\partial x_3} \sim Ri_{b,0} \frac{\partial \rho'}{\partial x_1}, \quad (6.4)$$

$$2\Omega_0 (s'_{13} + r'_{13}) \sim Ri_{b,0} \frac{\partial \rho'}{\partial x_2}, \quad 2\Omega_0 (s'_{23} + r'_{23}) \sim -Ri_{b,0} \frac{\partial \rho'}{\partial x_1}, \quad (6.5)$$

$$\underbrace{2\Omega_0 \omega'_1 s'_{13}}_{A1} + \underbrace{\Omega_0 \omega'_1 \omega'_2}_{B1} \sim \underbrace{Ri_{b,0} \omega'_1 \frac{\partial \rho'}{\partial x_2}}_{C1}, \quad \underbrace{2\Omega_0 \omega'_2 s'_{23}}_{A2} - \underbrace{\Omega_0 \omega'_1 \omega'_2}_{B2} \sim \underbrace{-Ri_{b,0} \omega'_2 \frac{\partial \rho'}{\partial x_1}}_{C2}. \quad (6.6)$$

When rotation is rapid, the tilting of planetary vorticity terms (A1 and A2) tend to be small relative to the coordinate system rotation terms (B1 and B2). The rotation term acts to transfer enstrophy from one horizontal component to another, but does not generate or destroy enstrophy. Owing to balance with the rotation term in rapidly rotating strongly stratified flow, baroclinic torque also acts to transfer enstrophy from one horizontal component to the other. In the present flow,  $\omega'_1 \omega'_2$  tends to be positive because mean strain increases horizontal enstrophy via vortex stretching, as in term  $VS\_MS$  in (6.1). Baroclinicity therefore should transfer from streamwise to lateral enstrophy as observed here, consistent with figure 12 of Part 1 with negative rotation rate.

## 7. Quantifying fluctuations

The dynamics of the stratified cases differ greatly from one another owing to differences in system rotation. Significant disorder is observed in the vorticity and scalar (not shown) fields when rotation is moderate and anticyclonic. In this section, the primary focus will be on quantitative differences between the stratified high- $Re$  cases with an emphasis on metrics that quantify the nature of turbulence. For the stratified cases, the centreline buoyancy Reynolds number,  $Re_B = \varepsilon(x_2 = 0)/\nu N^2$

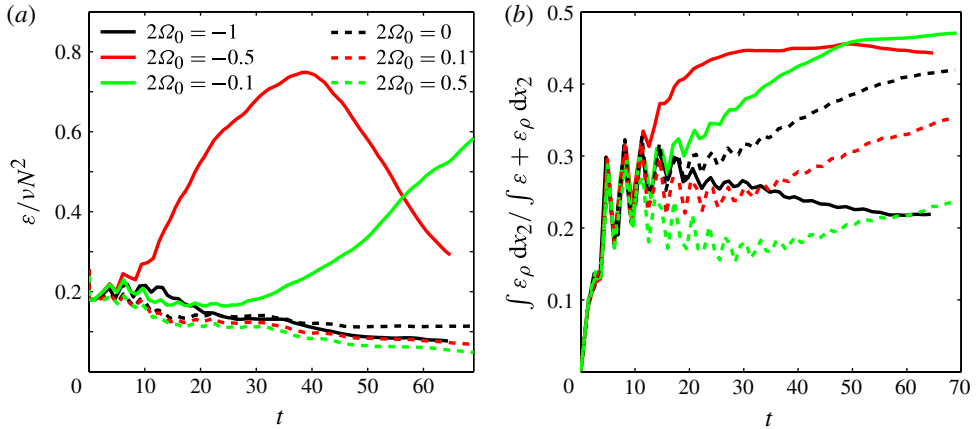


FIGURE 18. (Colour online) (a) Buoyancy Reynolds number and (b) the ratio of dissipation of potential energy to dissipation of both kinetic and potential energies versus time for the stratified cases.

where  $\varepsilon = 2\nu\langle s'_{ij}s'_{ij} \rangle$ , is plotted in figure 18(a). The  $2\Omega_0 = -0.1$  and  $-0.5$  cases are much more dissipative, but the buoyancy Reynolds number does not exceed unity. The  $2\Omega_0 = -1$ ,  $0.1$  and  $0$  cases have similar magnitudes of  $Re_B$  with the  $2\Omega_0 = -1$  and  $0.1$  cases being remarkably similar. The low values of  $Re_B$  in the weak and moderate anticyclonic cases contrast with evidence presented in the prior sections that the flow in these cases has a plethora of small-scale activity and that nonlinear terms are very important in enstrophy budgets.

Although values of  $Re_B$  are quite low, in figure 18(b) we see that dissipation of potential energy,  $\varepsilon_\rho$ , is the same order as dissipation of kinetic energy,  $\varepsilon$ , for the weak and moderate anticyclonic stratified cases. The high values are suggestive of high mixing efficiency for these flows, while lower mixing efficiency is expected for cyclonic and/or rapid rotation. The values for the non-rotating stratified case at  $Re_0 = 2400$  are greater than the lower- $Re_0$  stratified case of Basak & Sarkar (2006) as well as case  $Ri1NRe600$  with  $Re_0 = 600$  simulated here. Evidently, strongly stratified non-rotating flows can also have strong vertical mixing if the Reynolds number is sufficiently large as hypothesized previously (Riley & de Bruyn Kops 2003). We also explored the behaviour of  $Sk$ , the skewness of  $\partial u'_1/\partial x_1$ , which gives information relating to vortex stretching and energy transfer between scales. Note that isotropic unstratified turbulence has  $Sk \sim -0.45$ . For  $Ri0A10$  and  $Ri1A10$  the skewness is observed to be  $-0.44$  and  $-0.29$ , respectively, at the end of the simulation. The skewness of  $Ri1N$  and  $Ri1A1$  is very different, taking the values  $0.16$  and  $0.38$ , respectively. Therefore it is reasonable to conclude from the specific metric of skewness of  $\partial u'_1/\partial x_1$  that, at the high stratifications considered here, the high-rotation cases are not turbulent in the sense of three-dimensional turbulence in a homogeneous fluid. The anticyclonic cases with weak rotation, however, are most likely to be turbulent in that sense.

The quasi-two-component nature of the fluctuations in the stratified cases is shown in figures 19(a) and 19(b) while density variance is shown in figure 19(c). Vertical turbulent kinetic energy (TKE) is typically about two orders of magnitude smaller than horizontal TKE. The largest vertical TKE is observed for the weakly and moderately anticyclonic cases, while the rapidly rotating anticyclonic case exhibits

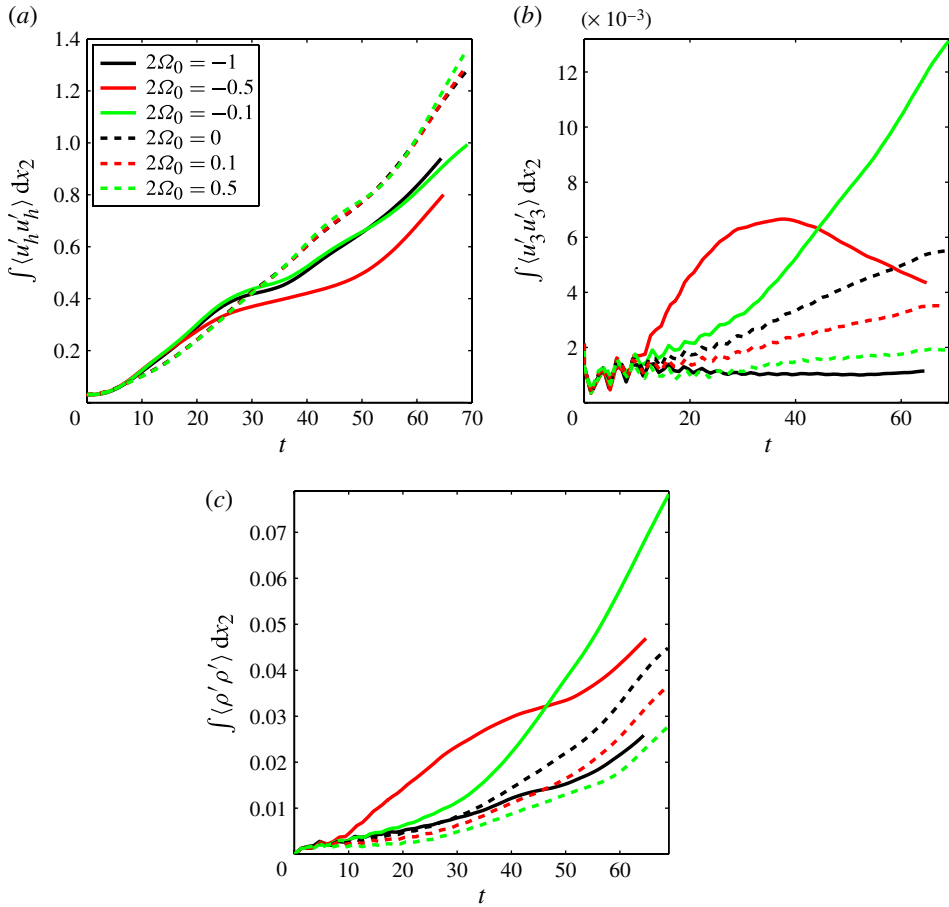


FIGURE 19. (Colour online) Integrated components of (a) horizontal and (b) vertical turbulent kinetic energy in addition to (c) density variance.

the smallest vertical TKE. Other quantities suggestive of turbulence are viscous dissipation and vortex stretching which are not shown, but give a general trend of strong destabilization initially for the anticyclonic cases with strong stabilization later in the  $2\Omega_0 = -1$  case.

Figure 20 shows the streamwise spectra at the end of each simulated case. As stated in § 2, initial spectra are identical in all cases. In general, the unstratified cases have the most energy at the smallest scales and the stratified non-rotating, cyclonic and strongly anticyclonic cases contain the least. The weaker anticyclonic stratified cases have small-scale energy at levels between the unstratified and other stratified cases. Case *Ri1A2* shows less energy in the intermediate wavenumbers than the more stable cases while still having significant energy in the smallest scales. This is likely to be due to the stabilizing effect of rotation on larger scales once  $t \gtrsim 13$  and active fine scales maintaining energy at the expense of the intermediate scales.

### 8. Conclusions

Part 1 investigated the three-dimensional instability of a stratified and rotating horizontally oriented shear layer with a hyperbolic-tangent velocity profile. The present

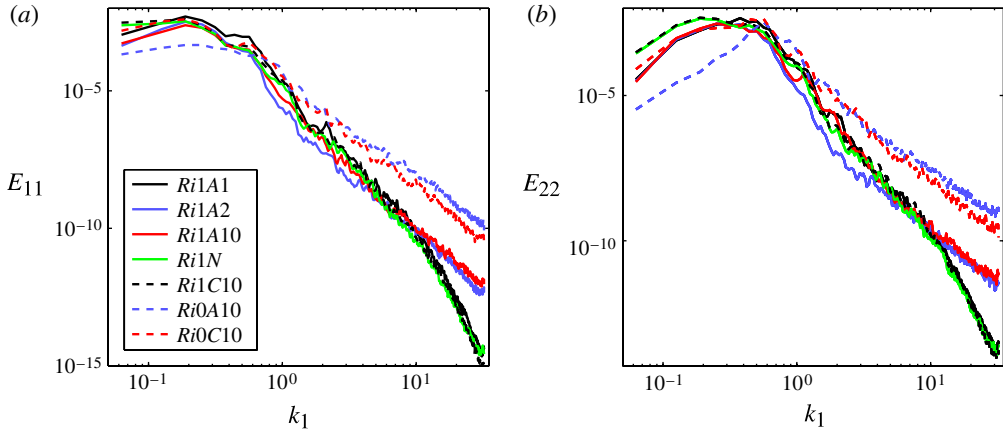


FIGURE 20. (Colour online) Plots of streamwise spectra at the end of each high- $Re_0$  simulation.

work, Part 2, is an exploration of the nonlinear evolution of the shear layer for  $|2\Omega| \sim O(1)$  focusing on strongly stratified flow with  $Ri_b(t) \geq 1$ . The cases have a Reynolds number based on vorticity thickness, initially at  $Re_0 = 2400$ , that increases to approximately  $Re = 16\,800$  at the end of the simulations, and are simulated using nearly 1 billion grid points. Although, cases with a lower  $Re_0 = 600$  are also simulated, the bulk of the presented results pertain to the higher- $Re$  series.

Visualizations of coherent vortex dynamics demonstrated that the qualitative differences between anticyclonic and cyclonic rotation at weak rotation persist in cases with strong stratification and also showed the importance of the buoyancy-induced instability, a modified barotropic mode at zero absolute vorticity, that was found in Part 1. During the initial evolution, the quasi-vertical vortices deform the fastest in the state with zero absolute vorticity at the centreline, and next fastest in the  $2\Omega_0 = -0.5$  case. This implied that the loss of cyclostrophic balance when  $2\Omega(t) = -1$  is more destabilizing to vortex cores than the initial influence of the inertial instability. The stratified  $2\Omega_0 = -1$  case shows deformation of the barotropic modes along the  $x_1$ - $x_3$  plane, consistent with the formation of lateral vorticity,  $\omega_2$ , by baroclinic effects when the absolute vorticity is zero. Vorticity dynamics show secondary KH shear instabilities during the evolution of the inertial instability when  $2\Omega(t) \approx -0.5$ . Also, the zero absolute vorticity instability possesses a vorticity signature distinct from the inertial instability.

As the  $2\Omega_0 = -0.1$  and  $-0.5$  cases progressed, a network of braid vortices formed and remained throughout the duration of both cases, even though  $2|\Omega(t)|$  attained values as large as 2.7. The cyclonic rotation cases with  $2\Omega_0 = 0.1$  and 0.5 did not show such braid vortices and, instead, exhibited behaviour very similar to the non-rotating case, but with vertical variability suppressed with increasing cyclonic rotation. The simulations at  $Re_0 = 600$  and  $Ri_{b,0} = 1$  exhibit initial deformation of the vortex cores similar to that at higher  $Re$  but, in strong contrast, do not show development of a network of braid vortices.

The shear layer thickens in the cross-stream direction owing to barotropic instabilities and turbulence. In the cases without stratification and with anticyclonic rotation, the thickening of the shear layer reduces to zero when the mean absolute vorticity approaches zero, consistent with the finding of Métais *et al.* (1995) and

the arguments of Kloosterziel *et al.* (2007a). In contrast, the stratified case continues to thicken beyond the zero absolute vorticity state. The enhanced horizontal stirring by the quasi-two-dimensional dynamics in the stratified case combined with the presence of the zero absolute vorticity instability and associated baroclinic generation of enstrophy fluctuations allows continued reduction of horizontal mean shear by turbulent fluctuations.

Fluctuating enstrophy statistics elucidated dynamically distinct features of the various rotation regimes. Horizontal enstrophy dominated in anticyclonic cases with weak rotation ( $2\Omega_0 = -0.1, -0.5$ ). Generation of horizontal enstrophy by nonlinear vortex stretching was substantial relative to the other terms in all cases; generation by vertical vortex stretching was only significant for intermediate rotation rates ( $-0.5 \gtrsim 2\Omega(t) \gtrsim -3$ ). Baroclinic torque changed from a sink to a source of  $\omega'_2$  fluctuations immediately after passing through the zero absolute vorticity state, as expected from the behaviour of linear barotropic modes in Part 1. Examination of the balance of terms in the transport equation for  $\omega'_2$  shows the important role of baroclinic production in allowing vorticity fluctuations to intensify after passing into the inertially stable regime.

The simulations are diagnosed for the state of velocity fluctuations. While the enstrophy budgets indicate that the flow is turbulent, buoyancy Reynolds numbers are very low, never exceeding unity even for the most unstable stratified cases. Mixing efficiency, inferred from dissipation of TKE and TPE, tends towards values on the order of 45% in the high-Reynolds-number stratified series when rotation is destabilizing, somewhat smaller values in the case without rotation, and significantly lower values for stabilizing rotation. Skewness of velocity derivative is also suggestive of nonlinearity associated with three-dimensional turbulence in the cases with moderate anticyclonic rotation. All stratified cases with or without rotation are in a high-stratification regime in the sense of being quasi-two-component, with more than 95% of turbulent kinetic energy being horizontal. Lastly, streamwise spectra are much shallower for the inertially unstable cases, albeit not nearly as shallow as the unstratified cases.

## Acknowledgements

The authors are pleased to acknowledge support by the National Science Foundation CDI program through Grant No. OCE-0835839. The authors also are grateful for computational resources through the Triton Affiliations and Partners Program at San Diego Supercomputing Center and a computing allocation through the Extreme Science and Engineering Discovery Environment (XSEDE).

## REFERENCES

- AFANASYEV, Y. D. & PELTIER, W. R. 1998 The three-dimensionalization of stratified flow over two-dimensional topography. *J. Atmos. Sci.* **55**, 19–39.
- AROBONE, E. & SARKAR, S. 2010 The statistical evolution of a stratified mixing layer with horizontal shear invoking feature extraction. *Phys. Fluids* **22**, 115108.
- AROBONE, E. & SARKAR, S. 2012 Evolution of a stratified rotating shear layer with horizontal shear. Part I. Linear stability. *J. Fluid Mech.* **703**, 29–48.
- BARTELLO, P., MÉTAIS, O. & LESIEUR, M. 1994 Coherent structures in rotating three-dimensional turbulence. *J. Fluid Mech.* **273**, 1–29.
- BASAK, S. & SARKAR, S. 2006 Dynamics of a stratified shear layer with horizontal shear. *J. Fluid Mech.* **568**, 19–54.

- BILLANT, P. & CHOMAZ, J.-M. 2000 Experimental evidence for a new instability of a vertical columnar vortex pair in a strongly stratified fluid. *J. Fluid Mech.* **418**, 167–188.
- CARNEVALE, G. F., KLOOSTERZIEL, R. C., ORLANDI, P. & VAN SOMMEREN, D. D. J. A. 2011 Predicting the aftermath of vortex breakup in rotating flow. *J. Fluid Mech.* **669**, 90–119.
- FLAMENT, P., LUMPKIN, R., TOURNADRE, J. & ARMI, L. 2001 Vortex pairing in an unstable anticyclonic shear flow: discrete subharmonics of one pendulum day. *J. Fluid Mech.* **440**, 401–409.
- JEONG, J. & HUSSAIN, F. 1995 On the identification of a vortex. *J. Fluid Mech.* **285**, 69–94.
- KLOOSTERZIEL, R. C., CARNEVALE, G. F. & ORLANDI, P. 2007a Inertial instability in rotating and stratified fluids: barotropic vortices. *J. Fluid Mech.* **583**, 379–412.
- KLOOSTERZIEL, R. C. & VAN HEIJST, G. J. F. 1991 An experimental study of unstable barotropic vortices in a rotating fluid. *J. Fluid Mech.* **223**, 1–24.
- KLOOSTERZIEL, R. C., ORLANDI, P. & CARNEVALE, G. F. 2007b Saturation of inertial instability in rotating planar shear flows. *J. Fluid Mech.* **583**, 413–422.
- LESIEUR, M., YANASE, S. & MÉTAIS, O. 1991 Stabilizing and destabilizing effects of a solid-body rotation on quasi-two-dimensional shear layers. *Phys. Fluids A* **3** (3), 403–407.
- MÉTAIS, O., FLORES, C., YANASE, S., RILEY, J. J. & LESIEUR, M. 1995 Rotating free-shear flows. Part 2. Numerical simulations. *J. Fluid Mech.* **293**, 47–80.
- OTHEGUY, P., BILLANT, P. & CHOMAZ, J.-M. 2006a Elliptic and zigzag instabilities on co-rotating vertical vortices in a stratified fluid. *J. Fluid Mech.* **553**, 253–272.
- OTHEGUY, P., BILLANT, P. & CHOMAZ, J.-M. 2006b The effect of planetary rotation on the zigzag instability of co-rotating vortices in a stratified fluid. *J. Fluid Mech.* **553**, 273–281.
- PLOUGONVEN, R. & ZEITLIN, V. 2009 Nonlinear development of inertial instability in a barotropic shear. *Phys. Fluids* **21**, 106601.
- POTYLITSIN, P. G. & PELTIER, W. R. 1998 Stratification effects on the stability of columnar vortices on the  $f$ -plane. *J. Fluid Mech.* **355**, 45–79.
- POTYLITSIN, P. G. & PELTIER, W. R. 1999 Three-dimensional destabilization of stuart vortices. *J. Fluid Mech.* **387**, 205–226.
- POTYLITSIN, P. G. & PELTIER, W. R. 2003 On the nonlinear evolution of columnar vortices in a rotating environment. *Geophys. Astrophys. Fluid Dyn.* **97**, 365–391.
- PRAUD, O., SOMMERIA, J. & FINCHAM, A. M. 2006 Decaying grid turbulence in a rotating stratified tank. *J. Fluid Mech.* **547**, 389–412.
- RILEY, J. J. & DE BRUYN KOPS, S. M. 2003 Dynamics of turbulence strongly influenced by buoyancy. *Phys. Fluids* **15** (7), 2047–2059.
- SMITH, L. M. & WALEFFE, F. 2002 Generation of slow large-scales in forced rotating stratified turbulence. *J. Fluid Mech.* **451**, 145–168.
- YANASE, S., FLORES, C., MÉTAIS, O. & RILEY, J. J. 1993 Rotating free-shear flows. I. Linear stability analysis. *Phys. Fluids* **5** (11), 2725–2737.